

Article

Chemometric Models of Differential Amino Acids at the Na_vα and Na_vβ Interface of Mammalian Sodium Channel Isoforms

Fernando Villa-Diaz ¹, Susana Lopez-Nunez ¹, Jordan E. Ruiz-Castelan ¹,
Eduardo Marcos Salinas-Stefanon ² and Thomas Scior ^{1,*} 

¹ Laboratory of Computational Molecular Simulations, Faculty of Chemical Sciences, BUAP, C.P. 72570 Puebla, Mexico; fer.vdl1928@gmail.com (F.V.-D.); susannalopez18@gmail.com or hefzi-ba@live.com.mx (S.L.-N.); toj_cdai90@live.jp (J.E.R.-C.)

² Institute of Physiology, BUAP, C.P. 72570 Puebla, Mexico; eduardo.salinas@correo.buap.mx

* Correspondence: tscior@gmail.com or thomas.scior@correo.buap.mx; Tel.: +52-222-2-295500 (ext. 7529)

Academic Editors: Humbert González-Díaz, Aliuska Duardo-Sanchez and Alejandro Pazos Sierra



Received: 1 June 2020; Accepted: 22 July 2020; Published: 3 August 2020

Abstract: (1) Background: voltage-gated sodium channels (Na_vs) are integral membrane proteins that allow the sodium ion flux into the excitable cells and initiate the action potential. They comprise an α (Na_vα) subunit that forms the channel pore and are coupled to one or more auxiliary β (Na_vβ) subunits that modulate the gating to a variable extent. (2) Methods: after performing homology in silico modeling for all nine isoforms (Na_v1.1α to Na_v1.9α), the Na_vα and Na_vβ protein-protein interaction (PPI) was analyzed chemometrically based on the primary and secondary structures as well as topological or spatial mapping. (3) Results: our findings reveal a unique isoform-specific correspondence between certain segments of the extracellular loops of the Na_vα subunits. Precisely, loop S5 in domain I forms part of the PPI and assists Na_vβ1 or Na_vβ3 on all nine mammalian isoforms. The implied molecular movements resemble macroscopic springs, all of which explains published voltage sensor effects on sodium channel fast inactivation in gating. (4) Conclusions: currently, the specific functions exerted by the Na_vβ1 or Na_vβ3 subunits on the modulation of Na_vα gating remain unknown. Our work determined functional interaction in the extracellular domains on theoretical grounds and we propose a schematic model of the gating mechanism of fast channel sodium current inactivation by educated guessing.

Keywords: homology modeling; extracellular loops; interactome; protein-protein interaction; hot spot prediction

1. Introduction

1.1. The Sodium Channels

Concerning the voltage-gated sodium channels (Na_vs), a plethora of genes, their reading frames, expression patterns and functions have been reported for various organisms ranging from prokaryotic to eukaryotic cells. We treat the isoforms of ion channels in vertebrates with their greater gene complexities [1,2].

The Na_v complex generally consists of a central α (Na_vα) subunit with the channel pore that is encoded by *SCN1A* to *SCN5A* (Na_v1.1α to Na_v1.5α, respectively) and *SCN8A* to *SCN11A* (Na_v1.6α to Na_v1.9α, respectively). The nine isoforms of the Na_vα subunit are expressed in specific tissue patterns and exhibit differences in gating behavior that adapts them to different physiological functions [3–6].

The pharmacological classification of these subtypes diverges according to their sensitivity and resistance to tetrodotoxin (TTX); $\text{Na}_v1.1\alpha$ to $\text{Na}_v1.4\alpha$, $\text{Na}_v1.6\alpha$ and $\text{Na}_v1.7\alpha$ are sensitive to blocking by low nanomolar concentrations of TTX (TTX-S) and $\text{Na}_v1.5\alpha$, $\text{Na}_v1.8\alpha$ and $\text{Na}_v1.9\alpha$ are resistant to concentrations $>1 \mu\text{M}$ TTX (TTX-R) [7].

More than a thousand point mutations have been identified in human Na_v s, while some of them have been associated with neurological, cardiovascular, muscular, and psychiatric disorders, such as epilepsy, arrhythmia, muscular paralysis, pain syndrome, and a broad spectrum in autism disorder [8–12].

Na_v s are targets for a wide variety of natural toxins and clinical therapeutic drugs [13–16].

1.2. The $\text{Na}_v\alpha$ Subunit

The $\text{Na}_v\alpha$ subunit of vertebrates consists of a single polypeptide chain with an approximate molecular mass of 260 kDa. It embraces the ion selective component that folds into four homologous but not identical domains (DI to DIV), each domain contains six transmembrane helical segments (S1 to S6), which are assembled around the ion selective pore [17,18].

The transmembrane helical segments S1, S2, S3, and S4 comprise the four voltage sensing domains (VSDs) in DI to DIV. They are located at the outer edge at each corner of the $\text{Na}_v\alpha$ subunit (Figure 1). The S4 helix constitutes the voltage sensor of each VSD. It has evolved into an amphipathic domain with a positively charged face. In response to the changes in the electric field produced by the depolarization of the membrane, the S4 moves towards the extracellular zone initiating conformational changes, which in turn open the pore [19–22]. The three S4 of the DI, DII, and DIII show faster kinetics in response to depolarization and allow sodium cations to enter the cells. The S4 of the DIV responds more slowly. Its movement releases an intracellular connector called the IFM inactivation gate. It contains three lipophilic residues (isoleucine, phenylalanine, methionine), and connects the S6 DIII to S1 DIV [23–25]. As a result, the inactivation gate moves to occlude the pore and leads the channel into an inactive state. Therefore, the activation and inactivation of the channel are linked in a structural, mechanical, and functional way [26,27].

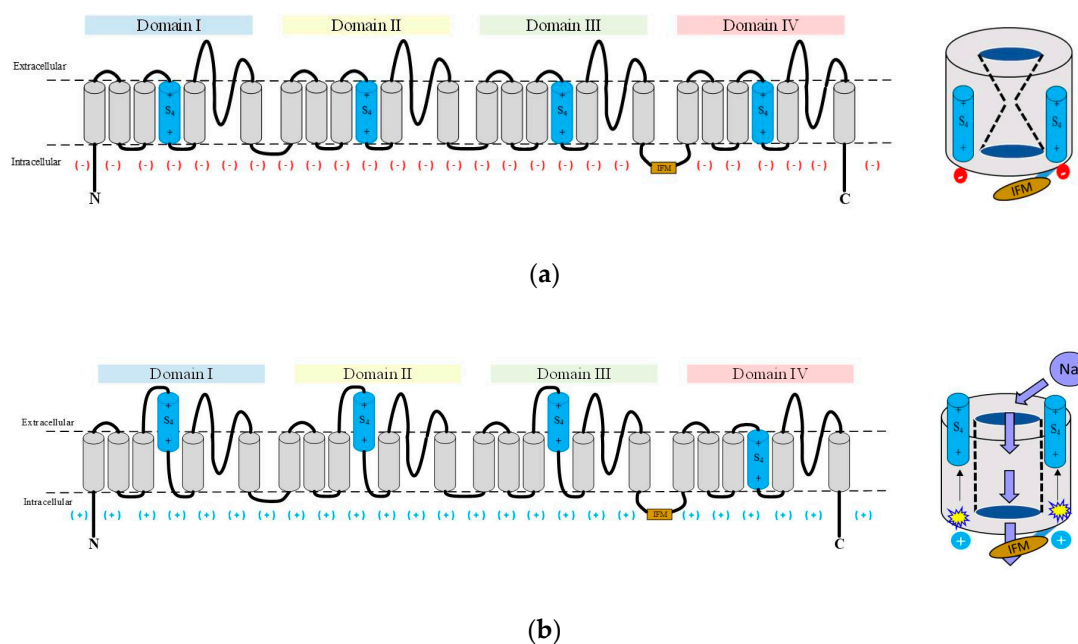


Figure 1. Cont.

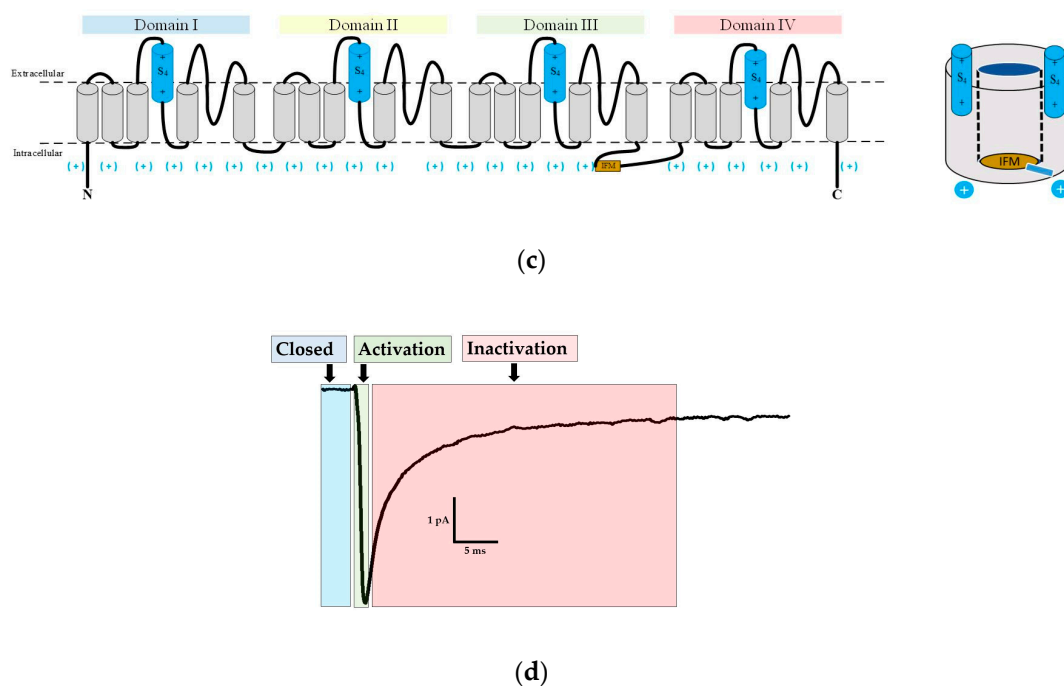


Figure 1. Schematic representation of gating. The three schemes of eukaryotic Na_vs show the (a) closed; (b) open; and (c) inactivated gating states. (d) A typical membrane current of *Rattus norvegicus* of the Na_vα1.4 isoform responds to a depolarizing pulse reflecting the three main states of gating; IFM inactivation gate: brownish; S4 voltage sensors: sky blue.

1.3. The Na_vβ Subunits

Most Na_vs of vertebrate cells form biological units with associated β subunits (Na_vβs). There are four Na_vβ genes (*SCN1B* to *SCN4B*) that encode four proteins Na_vβ1 to Na_vβ4, respectively [28,29]. Like the Na_vα subunits, the Na_vβ subunits are individually expressed for tissue differentiation [30,31].

While the Na_vα subunit is sufficient for voltage detection and selective ion conductance, the Na_vβs subunits modulate peak values of sodium current and modify the kinetics of the activation and inactivation of the Na_vα subunit. They increase peak current density by augmentation of the channel density (number per area) on the cell surface. They effectively change the voltage range involved in activation and inactivation and improve inactivation and recovery rates of inactivation [5,28,32–39].

Prior to this chemometric study we carried out electrophysiological and site-directed mutagenesis experiments combined with molecular modelling to study modulation of Na_vα subunit by Na_vβ1 [40–42].

All Na_vβ subunits are type 1 membrane proteins. The extra-cellular amino-terminal region contains a single V-type amino-terminal immunoglobulin domain (IgD) and a short neck connected to a transmembrane helix (TMH) in addition to a carboxy-terminal intracellular region. The sequences similarities between Na_vβ1 and Na_vβ3 are higher than between Na_vβ2 and Na_vβ4 [43,44]. Na_vβ1 and Na_vβ3 are linked to Na_vα through non-covalent interactions, while Na_vβ2 and Na_vβ4 are linked by a disulfide bridge with Na_vα [45,46].

The cryo-electron microscope (cryo-EM) structures of Na_vs of insects, electric eel, rat, or human species reveal an identical three-dimensional (3D) architecture of their Na_vα subunits. Comparing the interface between Na_vα and Na_vβ (Na_vα/Na_vβ) of electric eel as well as *Homo sapiens* reveals that it is astonishingly well conserved [47–52].

The identification of the interaction sites for modulation of the Na_vα subunit with the Na_vβ subunits mainly stems from the mutagenic analysis and structural information of the individual Na_vβ subunits [36,40–42,46,49,53–58].

1.4. The Present Contributions

Currently, it remains an unanswered question how exactly the pore subunit ($\text{Na}_v\alpha$) is modulated by the $\text{Na}_v\beta 1$ and $\text{Na}_v\beta 3$ subunits. Our present chemometric study aims at describing mechanistic behavior at the $\text{Na}_v\alpha/\text{Na}_v\beta$ to shed light on the modulation by the nine isoforms ($\text{Na}_v1.1\alpha$ to $\text{Na}_v1.9\alpha$) comparing three Mammalian species, namely *Homo sapiens* (hNa_v), *Mus musculus* (mNa_v) and *Rattus norvegicus* (rNa_v). To this end, well-established *in silico* methods were applied, like multiple sequence alignments, structural determinations, amino acid properties analysis, the generation of homology models as well as molecular electrostatic potentials, which can be color coded and projected on the molecular surfaces (MEPS).

To suit our chemometric analysis, the pore-bearing α subunit is dissected in the following topological parts. Herein after the entire pore subunit will be denominated as $\text{Na}_v\alpha$ or α for short. It is in turn composed of three topological segments: (i) the extracellular part or region (ECR) with its 16 extracellular loops (ECLs); (ii) the transmembrane helical part (TMH); and finally (iii) the intracellular region.

On theoretical ground, we determined (3D) structural features and sequence patterns as well as atom properties to describe the protein-protein interactions (PPI) between two pairs of proteins: not only $\text{Na}_v\alpha$ with $\text{Na}_v\beta 1$ subunits ($\text{Na}_v\alpha/\text{Na}_v\beta 1$) but also $\text{Na}_v\alpha$ with $\text{Na}_v\beta 3$ subunits ($\text{Na}_v\alpha/\text{Na}_v\beta 3$). The term PPI implies that both pairs were always treated in parallel for all three Mammalian species to provide a total and systematic view on chemometric patterns. While the (3D) structures of the former pair have been experimentally elucidated (by cryo-electron microscopy or crystallography), no (3D) structural information exists for the latter pair. This means, on the one hand we studied existing $\text{Na}_v\alpha/\text{Na}_v\beta 1$ complexes, while on the other hand we directly applied our findings to create a hitherto unknown interface (symbol /) between $\text{Na}_v\alpha$ with $\text{Na}_v\beta 3$ ($\text{Na}_v\alpha/\text{Na}_v\beta 3$). Herein after, the observed as well as the postulated interface will be denominated as IF, for short. The ectodomain of said IF contains the extracellular loops of the $\text{Na}_v\alpha$ subunit, which will be called ECLs in our study. All those (short) ECL segments in interaction with $\text{Na}_v\beta 1$ or $\text{Na}_v\beta 3$ subunits will be designated as IF-ECLs. All told, ECLs always belong to an α subunit, never to a β subunit because the latter does not possess loops, only antiparallel beta-strands which bend in turns and hair pins to form ordered beta-sheets (immunoglobulin domain, IgD, or all-beta fold). Finally, IF-ECLs embrace short amino acid segments, sometimes only a few individual residues, which we studied at either a sequential or even atomic scale.

2. Results

2.1. Determination of PPI in the Isoforms of the Na_v s

Our chemometric study produced detailed data, a fairly larger portion of which we present in the Supplementary Materials section. Precisely, the observed as well as the computed property patterns of interacting residues at the interface were described for eight PPI patches (thereupon called PPI-Id) by nine isoforms of three species for two pairs ($\text{Na}_v\alpha/\text{Na}_v\beta 1$ and $\text{Na}_v\alpha/\text{Na}_v\beta 3$), all of which yields 832 PPIs in 27 3D models ($8 \times 9 \times 3 \times 2$) based on known 3D structures. When we take into account the four domains on each α subunit, the pore chain and the fact that each of those four domains (D1 to DIV) exposes four ECLs, then the sheer amount of 432 sets of calculations ($16 \text{ loops} \times 9 \text{ isoforms} \times 3 \text{ species}$) were prepared, carried out, gathered, documented and interpreted. Table 1 provides a synopsis about the obtained results describing the interaction between $\text{Na}_v\alpha/\text{Na}_v\beta 1$ or $\text{Na}_v\alpha/\text{Na}_v\beta 3$. Of note, eight different computed polar interaction patterns were identified across all four domains (DI to DIV). They extend by far the extant literature for its systematic analysis and completeness (cf. 2.1.1.).

Table 1. Synopsis of the studied PPI patterns. The interaction sites are labeled as **PPI-Id** with Arabic numerals from “1” to “8” to identify them. The resulting patterns are labeled with Roman numerals from “I” to “IX”. Certain PPI between $\text{Na}_v\alpha/\text{Na}_v\beta 1$ and $\text{Na}_v\alpha/\text{Na}_v\beta 3$ have been observed experimentally by structure elucidation. Their respective PDB entries and PPI-Id values are marked in bold face. They were used as templates for the reminder. The Y/N values in the table cells symbolize YES/NO referring to the presence / absence of contributions to PPI.

Isoform	IF-ECLs ⁶	S5 DI		S1-S2 DIII		S5 DIV	S6 DIV			PPI Pattern
	PPI-Id ³	1	2	3	4	5	6	7	8	
$\text{hNa}_v1.1\alpha$ ⁵	P35498 ²	Y	Y	Y	Y	Y	N	Y	Y	I
$\text{mNa}_v1.1\alpha$ ⁵	A2APX8 ²	Y	Y	Y	Y	Y	N	Y	Y	I
$\text{rNa}_v1.1\alpha$ ⁵	P04774 ²	Y	Y	Y	Y	Y	N	Y	Y	I
$\text{hNa}_v1.2\alpha$ ⁴	6J8E ¹	Y	Y	Y	Y	Y	Y	Y	Y	II
$\text{mNa}_v1.2\alpha$ ⁵	B1AWN6 ²	Y	Y	Y	Y	Y	Y	Y	Y	II
$\text{rNa}_v1.2\alpha$ ⁵	P04775 ²	Y	Y	Y	Y	Y	Y	Y	Y	II
$\text{hNa}_v1.3\alpha$ ⁵	Q9NY46 ²	Y	Y	Y	Y	Y	N	Y	Y	I
$\text{mNa}_v1.3\alpha$ ⁵	A2ASI5 ²	Y	Y	Y	Y	Y	N	Y	Y	I
$\text{rNa}_v1.3\alpha$ ⁵	P08104 ²	Y	Y	Y	Y	Y	N	Y	Y	I
$\text{eeNa}_v1.4\alpha$ ⁴	5XSY ¹	N	Y	Y	Y	Y	Y	Y	Y	IX
$\text{hNa}_v1.4\alpha$ ⁴	6AGF ¹	Y	Y	Y	Y	Y	Y	Y	Y	II
$\text{mNa}_v1.4\alpha$ ⁵	Q9ER60 ²	Y	Y	Y	Y	Y	Y	Y	Y	II
$\text{rNa}_v1.4\alpha$ ⁵	P15390 ²	Y	Y	Y	Y	Y	Y	Y	Y	II
$\text{hNa}_v1.5\alpha$ ⁵	Q14524 ²	Y	Y	N	Y	Y	N	Y	Y	III
$\text{mNa}_v1.5\alpha$ ⁵	Q9JJV9 ²	Y	Y	N	Y	Y	N	Y	Y	III
$\text{rNa}_v1.5\alpha$ ⁴	6U70 ¹	Y	Y	N	Y	Y	N	Y	Y	III
$\text{hNa}_v1.6\alpha$ ⁵	Q9UQD0 ²	Y	Y	Y	Y	Y	Y	Y	Y	II
$\text{mNa}_v1.6\alpha$ ⁵	Q9WTU3 ²	Y	Y	Y	Y	Y	Y	Y	Y	II
$\text{rNa}_v1.6\alpha$ ⁵	O88420 ²	Y	Y	Y	Y	Y	Y	Y	Y	II
$\text{hNa}_v1.7\alpha$ ⁴	6J8G ¹	Y	Y	Y	Y	Y	N	Y	Y	I
$\text{mNa}_v1.7\alpha$ ⁵	Q62205 ²	Y	Y	Y	Y	Y	N	Y	Y	I
$\text{rNa}_v1.7\alpha$ ⁵	O08562 ²	Y	Y	Y	Y	Y	N	Y	Y	I
$\text{hNa}_v1.8\alpha$ ⁵	Q9Y5Y9 ²	Y	Y	Y	N	Y	N	Y	Y	IV
$\text{mNa}_v1.8\alpha$ ⁵	Q6QIY3 ²	Y	Y	N	N	Y	N	Y	Y	V
$\text{rNa}_v1.8\alpha$ ⁵	Q62968 ²	Y	N	N	N	Y	N	Y	Y	VI
$\text{hNa}_v1.9\alpha$ ⁵	Q9UI33 ²	Y	N	Y	N	Y	N	N	N	VII
$\text{mNa}_v1.9\alpha$ ⁵	Q9R053 ²	Y	Y	N	N	Y	N	N	N	VIII
$\text{rNa}_v1.9\alpha$ ⁵	O88457 ²	Y	Y	N	N	Y	N	N	N	VIII

¹ PDB entry (<http://www.rcsb.org/>); ² UniProt code (<https://www.uniprot.org/>); ³ PPI-Id for computed polar interactions between $\text{hNa}_v\alpha$ and $\text{hNa}_v\beta$ subunits (Table S1, Supplementary Materials); ⁴ homology-modeled and refined structures (3D templates), see Table S1; ⁵ models; ⁶ ECLs which form interfaces with $\text{Na}_v\beta 1$ or $\text{Na}_v\beta 3$ are called IF-ECLs; Y: Interaction; N: No interaction; $\text{eeNa}_v1.4\alpha$: *Electrophorus electricus* $\text{Na}_v1.4\alpha$ isoform; labels I to XI: Groups of PPI patterns.

In Table 1 nine PPI patterns (Roman numerals) were detected as a result of the line-wise combination of Yes/No interaction features. Each line represents the eight identified potential contact zones in our study (PPI-Ids): (I) Id 6 has no PPI for hNa_v , mNa_v and rNa_v (1.1, 1.3 and 1.7); (II) Ids 1 to 8 have PPIs for hNa_v , mNa_v and rNa_v (1.2, 1.4 and 1.6); (III) Id 3 and 6 have no PPIs for hNa_v , mNa_v and rNa_v (1.5); (IV) Id 4 and 6 have no PPIs for $\text{hNa}_v1.8\alpha$; (V) Id 3, 4 and 6 have no PPI for $\text{mNa}_v1.8\alpha$; (VI) Id 2, 3, 4 and 6 have no PPI for $\text{rNa}_v1.8\alpha$; (VII) Id 2, 4, 6, 7 and 8 have no PPI for $\text{hNa}_v1.9\alpha$; (VIII) Id 3, 4, 6, 7 and 8 have no PPI for m , $\text{rNa}_v1.9\alpha$; (IX) Id 1 has no PPI for $\text{eeNa}_v1.4\alpha$.

2.1.1. PPI Analysis in the Structural Complex eeNav_v1.4α/eeNav_vβ1

Figure 2 presents the PPI for eeNav_v1.4α/eeNav_vβ1 (PDB: 5XSY [48]). Six interactions in three ECLs had already been published prior to our study: S1–S2 DIII, S5 DIV, and S6 DIV. However, our analysis of eel template unveiled a hitherto unpublished interaction site on ECL S5 DI (6 + 1 = 7 PPI-Ids).

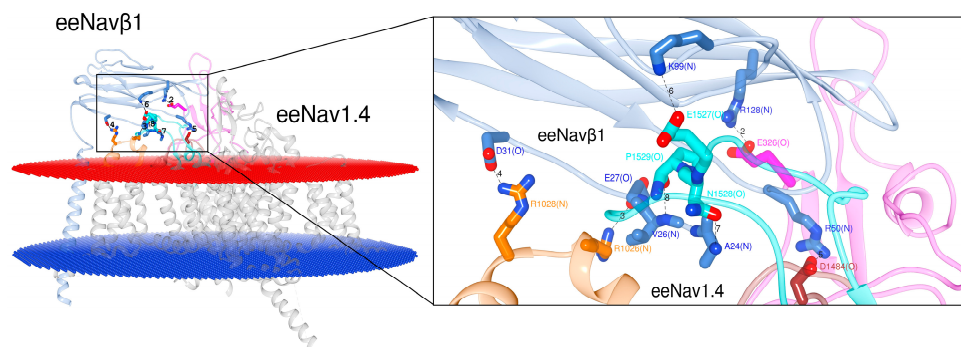


Figure 2. Display of the 3D model for S6 DIV in eeNav_v1.4α/eeNav_vβ1 [48]. The box displays details about the interacting residues at the interface. Labels 2 to 8: PPI identification numbers (PPI-Ids) of computed polar interactions (Table S1, Supplementary Materials); the amino acids are labeled by one-letter-codes with their primary sequence residue numbers and interacting atoms, e.g. A24(N). Colors: extracellular membrane boundaries (dark red); intracellular membrane boundaries (navy blue); transmembrane and intracellular protein regions of Na_vα which do not participate in PPI (gray); Na_vβ1 subunit (cornflower blue); S5 DI: magenta; S1–S2 DIII: orange; S5 DIV: brown; S6 DIV: cyan; computed polar interactions: black dotted lines. Visualization achieved by Chimera Alpha 1.14.

2.1.2. PPI Analysis of the hNav_v1.4α/hNav_vβ1 and hNav_v1.4α/hNav_vβ3 Models

The 3D template complexes eeNav_v1.4α/eeNav_vβ1 [48] and hNav_v1.4α/hNav_vβ1 [49] possess a significant sequence identity (Na_vα ≈ 65% and Na_vβ ≈ 46%, resp.) in addition to a relatively high degree of conserved residues by homology. A measure of geometrical deformation is the so-called root-mean-square deviation (RMSD). The PDB entries 5XSY [48] versus 6AGF [49] were compared in terms of RMSD for both subunits: Na_vα ≈ 0.942, Na_vβ ≈ 0.955. A first inspection of both 3D templates by eyesight also revealed how well-conserved are all IF-ECLs with Na_vβ1 between both species.

After the detection of the seventh PPI site (cf. 2.1.1.) we inspected the 3D template hNav_v1.4α/hNav_vβ1 [49] and our homology model hNav_v1.4α/hNav_vβ3 [49,55] (Figure 3). At this stage we detected another PPI site on the ECL S5 DI. Hereupon we label the six published and the two detected PPI sites as follows: PPI-Ids 3 to 8 and PPI-Ids 1 and 2, respectively. Of note, PPI-Ids 3 to 8 were observed on 3D template eeNav_v1.4α/eeNav_vβ1 [48]. Albeit, side chain rotation by Chimera's built-in rotamer library [59–61] had to be applied on the 3D template hNav_v1.4α/hNav_vβ1 [49]. Both detected PPI-Ids (1 and 2) lie on ECL S5 DI.

2.1.3. Identification of the Interacting Residues

Multiple sequence alignment (MSA) was performed by the Web-based Clustal Omega server [62] with the primary sequences of eeNav_v1.4α, hNav_v1.1α to hNav_v1.9α, mNav_v1.1α to mNav_v1.9α, rNav_v1.1α to rNav_v1.9α and all β subunits (eeNav_vβ1, hNav_vβ1 to hNav_vβ4, mNav_vβ1 to mNav_vβ4 and rNav_vβ1 to rNav_vβ4). We identified the conserved amino acids and replacements by homology since they constitute either structurally or functionally pivotal components for the channel (Table 2). As a most valuable asset, the hitherto known interacting residues of the 3D templates served as references to identify the interacting residues (Table 1 and Table S1). The 3D templates were as follows: eeNav_v1.4α/eeNav_vβ1, hNav_v1.4α/hNav_vβ1, and hNav_v1.4α/hNav_vβ3 (Figures 2 and 3).

On Na_vα two unchanged residues were detected in sequence positions labeled as PPI-Ids 1 and 5 on ECLs S5 DI and S5 DIV, respectively. On the counter subunit β, both subunits contain partially

conserved residues in positions PPI-Ids 2b, 3b, and 5b, but on PPI-Id 8b valine (V) remains unchanged. Intriguingly both β s also present two homologous residues by keeping their respective charges at positions 4 (negative) and 6 (positive) in all isoforms and species. In contrast, Table 2 also unravels that equivalent residues on $\text{Na}_v\beta 2$ or $\text{Na}_v\beta 4$ are not conserved when compared to locations on the three reference sequences of the $\text{eeNa}_v\beta 1$, $\text{hNa}_v\beta 1$ or $\text{hNa}_v\beta 3$ templates.

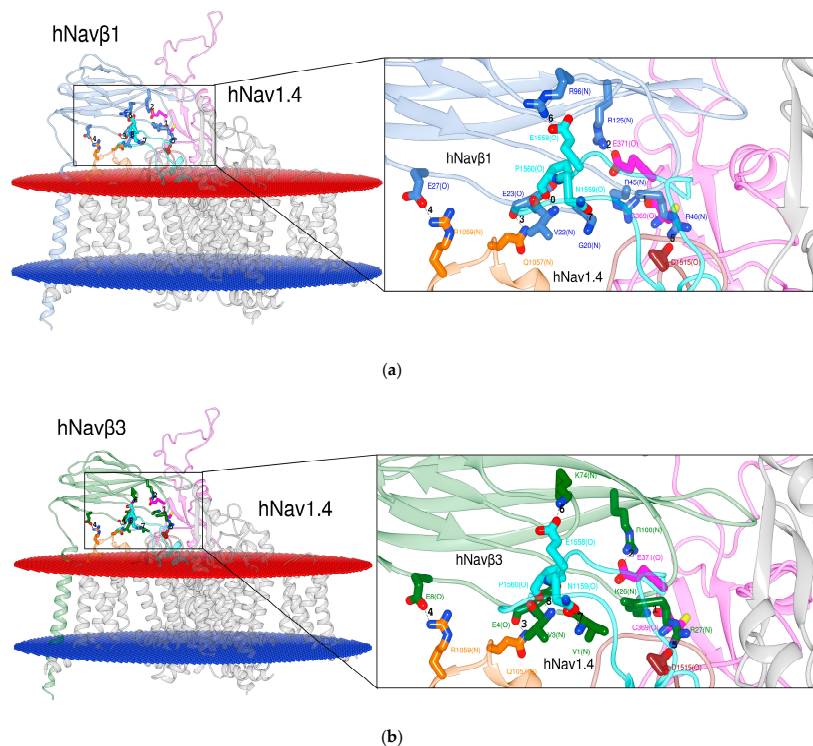


Figure 3. Display of PPI models. Based on the 3D template in (a) $\text{hNa}_v1.4\alpha/\text{hNa}_v\beta 1$ [49]; based on a homology model in (b) $\text{hNa}_v1.4\alpha/\text{hNa}_v\beta 3$ [49,55] for S6 DIV. The box presents atomic details at the interface. Labels 1 to 8: Ids of computed polar interactions (Table S1, Supplementary Materials); the amino acids are labeled by one-letter-codes with their primary sequence residue numbers and interacting atoms in parentheses, e.g. bottommost D1515(O). Colors: extracellular membrane boundaries (dark red); intracellular membrane boundaries (navy blue); transmembrane and intracellular protein regions of $\text{Na}_v\alpha$ that do not participate in PPI (gray); $\text{Na}_v\beta 1$ subunit (cornflower blue); $\text{Na}_v\beta 3$ subunit (forest green); S5 DI: magenta; S1-S2 DIII: orange; S5 DIV: brown; S6 DIV: cyan); computed polar interactions: black dotted lines. Visualization achieved by Chimera Alpha 1.14 [61].

In the following we describe two PPI-Id cases to illustrate how Table 1, Table 2 and Table S1 are combined with Figure 2, Figure 3 and Figures S1–S9. Take the upper leftmost corner of Table 1. The value in the cell for PPI-Id 1 of $\text{Na}_v1.1\alpha$ is “Y”, i.e. yes there is a PPI. This corresponds to cysteine (C) in Table S1 (first row entry of data crossed by 3rd col.: “agqCpeg(O)”. This corresponds to the string “agqCpEgym” which was generated by MSA in Table 2. Table S1 informs that C is in contact with arginine (R) of human $\text{Na}_v\beta 1$ (3rd col. under PPI-Id “1b” the value “R” in string “sckRrse(N)”). For this instance, the spatial configuration is depicted in atomic details (Figure S1). In this case the amide oxygen atom ($>\text{C}=\text{O}$) of cysteine forms a hydrogen bond with one nitrogen of β 's arginine. Table S1 informs about this PPI instance in a nongraphical way. The IF has two sides with PPI-Id 1 and PP-Id 1b. On the human pore subunit of isoform 1.1 ($\text{hNa}_v1.1\alpha$) the string value “agqCpeg(O)” reports that the interacting residue is cysteine (C). It interacts through its backbone oxygen atom (O). On the other side the Table S1 holds the string value “sckRrse(N)” at position PPI-Id “1b” for $\text{Na}_v\beta 1$. This means that arginine is the counterpart. On an atomic scale nitrogen atom(s) of its monocationic guanidinium head group from its side chain can establish the hydrogen bonding with a strong polar attraction.

Table 2. Multiple sequence alignments for either all nine α subunits or all four β subunits of three Mammalian organisms in addition to eel 3D template. MSA identified eight conserved or homologous residues on $\text{Na}_v\alpha$ and $\text{Na}_v\beta$. Asterisks (*) in first column: 3D template structures from PDB. Capital letters in bold face: the eight residues. Lower case letters: amino acid neighbors of the eight residues for numberless identification. Colors: positively and negatively charged residues in blue and red, respectively; polar or non-polar residues in cyan or orange.

Isoform	UniProt Code ¹	ECL			
		S5 DI 1, 2	S1-S2 DIII 3, 4	S5 DIV 5	S6 DIV 6, 7, 8
hNa _v 1.1 α	P35498	agqCpEgym	yidQrKtik	gidDmfn	pnkVNPgss
mNa _v 1.1 α	A2APX8	agqCpEgym	yidQrKtik	gidDmfn	pnkVNPgss
rNa _v 1.1 α	P04774	agqCpEgym	yidQrKtik	gidDmfn	pnkVNPgss
hNa _v 1.2 α	Q99250	agqCpEgyi	yieQrKtik	gidDmfn	pdkDHPgss
mNa _v 1.2 α	B1AWN6	agqCpEgyi	yieQrKtikd	gidDmfn	pekDHPgss
rNa _v 1.2 α	P04775	agqCpEgyi	yieQrKtik	gidDmfn	pekDHPgss
hNa _v 1.3 α	Q9NY46	agqCpEgyi	yieQrKtik	gidDmfn	pdtIHPgss
mNa _v 1.3 α	A2ASI5	agqCpEgyi	yieQrKtik	gidDmfn	pdaIHPgss
rNa _v 1.3 α	P08104	agqCpEgyi	yieQrKtik	gidDmfn	pdaIHPgss
* eeNa _v 1.4 α	P02719	agkCpEgyt	yiwRrRvik	gvdDifn	pdvENPgtd
* hNa _v 1.4 α	P35499	aghCpEgye	yieQrRvir	gidDmfn	pnlENPgts
mNa _v 1.4 α	Q9ER60	aghCpEgye	yieQrRvir	gidDmfn	ptlENPgtn
rNa _v 1.4 α	P15390	aghCpEgye	yieQrRvir	gidDmfn	ptlENPgtn
hNa _v 1.5 α	Q14524	agtCpEgyr	yleErKtik	gidDmfn	ptlPNSngs
mNa _v 1.5 α	Q9JJV9	agtCpEgyr	yleErKtik	gidDmfn	pnlPNSngs
rNa _v 1.5 α	P15389	agtCpEgyr	yleErKtik	gidDmfn	pnlPNSngs
hNa _v 1.6 α	Q9UQD0	agqCpEgyq	yieQrKtir	gidDmfn	ldkEHPgsg
mNa _v 1.6 α	Q9WTU3	agqCpEgfq	yieQrKtir	gidDmfn	ldkEHPgsg
rNa _v 1.6 α	O88420	agqCpEgfq	yieQrKtir	gidDmfn	ldkEHPgsg
hNa _v 1.7 α	Q15858	sgqCpEgyt	yieRkKtik	ginDmfn	pkkVHPgss
mNa _v 1.7 α	Q62205	sgqCpEgye	yieKkKtik	ginDmfn	pkkVHPgss
rNa _v 1.7 α	O08562	sgqCpEgyi	yieKkKtik	ginDmfn	pkkVHPgss
hNa _v 1.8 α	Q9Y5Y9	sghCpDgyi	yldQkPtvk	gidDmfn	pnlPNSngt
mNa _v 1.8 α	Q6QIY3	aghCpNdyv	yleEkPrvk	gidDmfn	pnrPNSngs
rNa _v 1.8 α	Q62968	aghCpGgyv	yleEkPrvk	gidDmfn	pnlPNSngs
hNa _v 1.9 α	Q9UI33	nsaCsIqye	hleNqPkiq	gidDifn	rskESCnss
mNa _v 1.9 α	Q9R053	rrsCpDgst	nlpSrPqve	gidDifn	eskASCnss
rNa _v 1.9 α	O88457	srpCpNgst	nlpSrPqve	gidDifn	eakEHCnss
Subunit	UniProt code ¹	7, 8, 3, 4	1,5	6	2
* eeNa _v β 1	A0A1L3MZ94	sngAcVEvdsDtea	sckMRgev	mgsKntf	yfdRtlf
* hNa _v β 1	Q07699	acgGcVEvdsEtea	sckRRset	ngsRgtk	hvyRllf
mNa _v β 1	P97952	awgGcVEvdsDtea	sckRRset	ngsRgtk	hvyRllf
rNa _v β 1	Q00954	awgGcVEvdsEtea	sckRRset	ngsRgtk	hvyRllf
* hNa _v β 3	Q9NY72	cfpVcVEvpsEtea	scmKReev	ngsKdlq	nvsRefe
mNa _v β 3	Q8BHK2	cfpVcVEvpsEtea	scmKReev	ngsKdlq	nvsRefe
rNa _v β 3	Q9JK00	cfpVcVEvpsEtea	scmKReev	ngsKdlq	nvsRefe
hNa _v β 2	O60939	grsMeVTvpaTlnv	fnsCYtn	sgnPsky	yimNppd
mNa _v β 2	Q56A07	grsMeVTaptTlsv	fnsCYtn	sgnPsky	yitNppd
rNa _v β 2	P54900	grsMeVTvptTlsv	fnsCYtn	sgnPsky	yitNppd
hNa _v β 4	Q8IWT1	sleVsVGkatDiya	fssCFgfe	vgsTkek	hvkNpke
mNa _v β 4	Q7M729	sleVsVGkatTiya	fssCYgfe	egsTkek	fvrNpke
rNa _v β 4	Q7M730	sleVsVGkatTiya	fssCYgfe	egsTkek	fvrNpke

¹ <https://www.uniprot.org>.

The Table 1 in its bottommost rightmost corner informs that no (value “N”) exists for PPI-Id 8 in case of rNa_v1.9 α . Again, Table S1 lends insight not only on a molecular level but also at an atomic scale. The 1.9 isoform’s subunit α has a potential contribution by a cysteine at sequence position PPI-Id 8 (“kehCnss”), but the counter subunits (Na_v β) present a nonresponding valine (V). This aliphatic residue is conserved on all four β subunits. As a direct result Table 1 summarizes this negative interaction with an “N” qualifier in its corresponding table cell along with all other “Yes” or “No” contributions for the systematic combinations of three Mammalian species, nine isoforms and eight potential PPI sites (labeled PPI-Ids 1 to 8). The two detailed illustrations underline the informative wealth of chemometric studies to complement limited experimental data. They do, however, also raise the molecular modeling practitioner’s challenges concerning management and presentation of data in huge volumes.

2.1.4. Structure Alignment of all Na_v β s Subunits

Figure 4 displays the results of the (3D) structure alignment (SA), i.e., the ectodomain (IgD) superpositions in space for the 3D templates, namely the cryo-EM structures of eeNa_v β 1, hNa_v β 1 in addition to the crystal structures of hNa_v β 2 to hNa_v β 4 (PDB: 5XSY [48], 6AGF [49], 5FEB [56], 4L1D [55], and 4MZ2 [54]).

The SA of the subunits eeNa_v β 1 and hNa_v β 1 provides a visual means to identify the interacting residues for eeNa_v1.4 α /eeNa_v β 1 [48] (Figure 2). As can be noticed, essential features remain in close spatial proximity while keeping their properties, except for one of the eight interaction sites: PPI-Id 1 (Figure 4a).

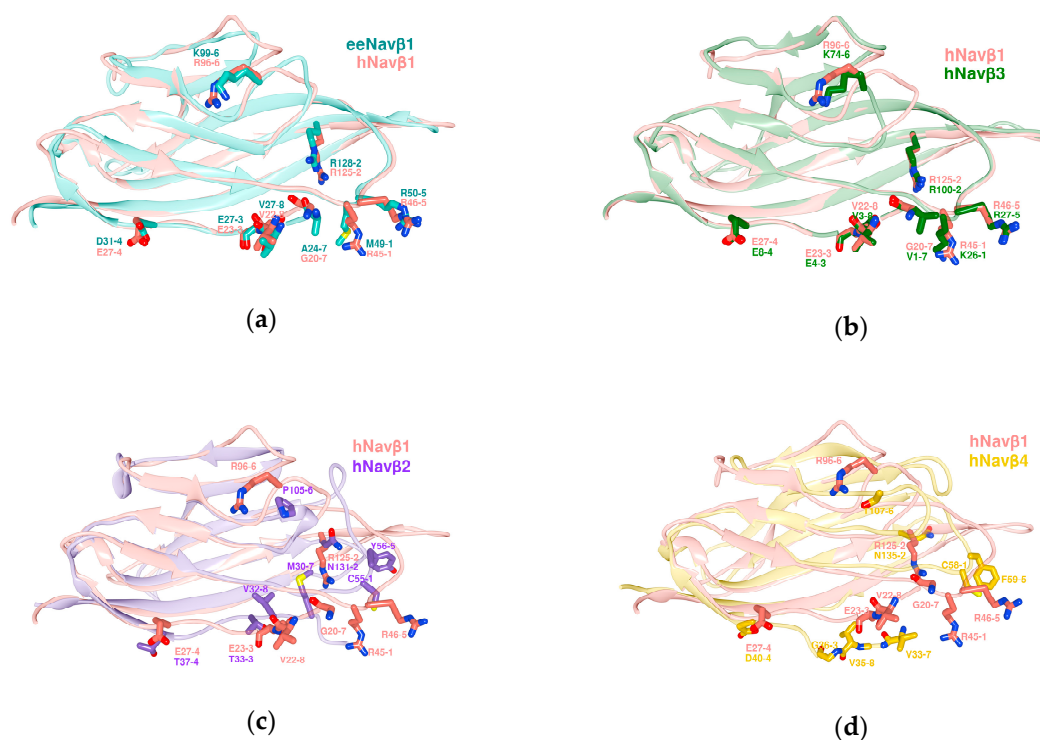


Figure 4. Structure alignments of the ectodomains (IgD) of β subunit templates. (a) eeNa_v β 1 with hNa_v β 1; (b) hNa_v β 1 with hNa_v β 3; (c) hNa_v β 1 with hNa_v β 2; (d) hNa_v β 1 with hNa_v β 4; eeNa_v β 1: sea green; hNa_v β 1: salmon; hNa_v β 3: forest green; hNa_v β 2: purple; hNa_v β 4: golden; labels 1 to 8: positions of MSA residues according to Table 2. All superpositions were achieved by Chimera Alpha 1.14 with MatchMaker [61].

2.2. Pore Modulation by Na_v β Concerning the Acceleration for Fast Gating Inactivation

Our hypothesis has been based on the displacement of S4 DIII towards the extracellular region during cell membrane depolarization, when it contacts Na_v β 1 or Na_v β 3 (Figure 5). It is not far-fetched

to assume that if a voltage sensor gets close enough for noncovalent binding with IgD ectodomains, a spatial rearrangement will take place. Surface charges on $\text{Na}_v\alpha$ will come under the influence of positively charged lysines (K37 on $\text{Na}_v\beta 1$ or K18 on $\text{Na}_v\beta 3$, see our Table S2, cf. Figure 4c,d in [49,55]). Consequently, this displacement could trigger modulation of the pore subunit ($\text{Na}_v\alpha$). Furthermore, we assume that this contact exerts a domain rotation that affects the fast inactivation of $\text{Na}_v\alpha$ gating.

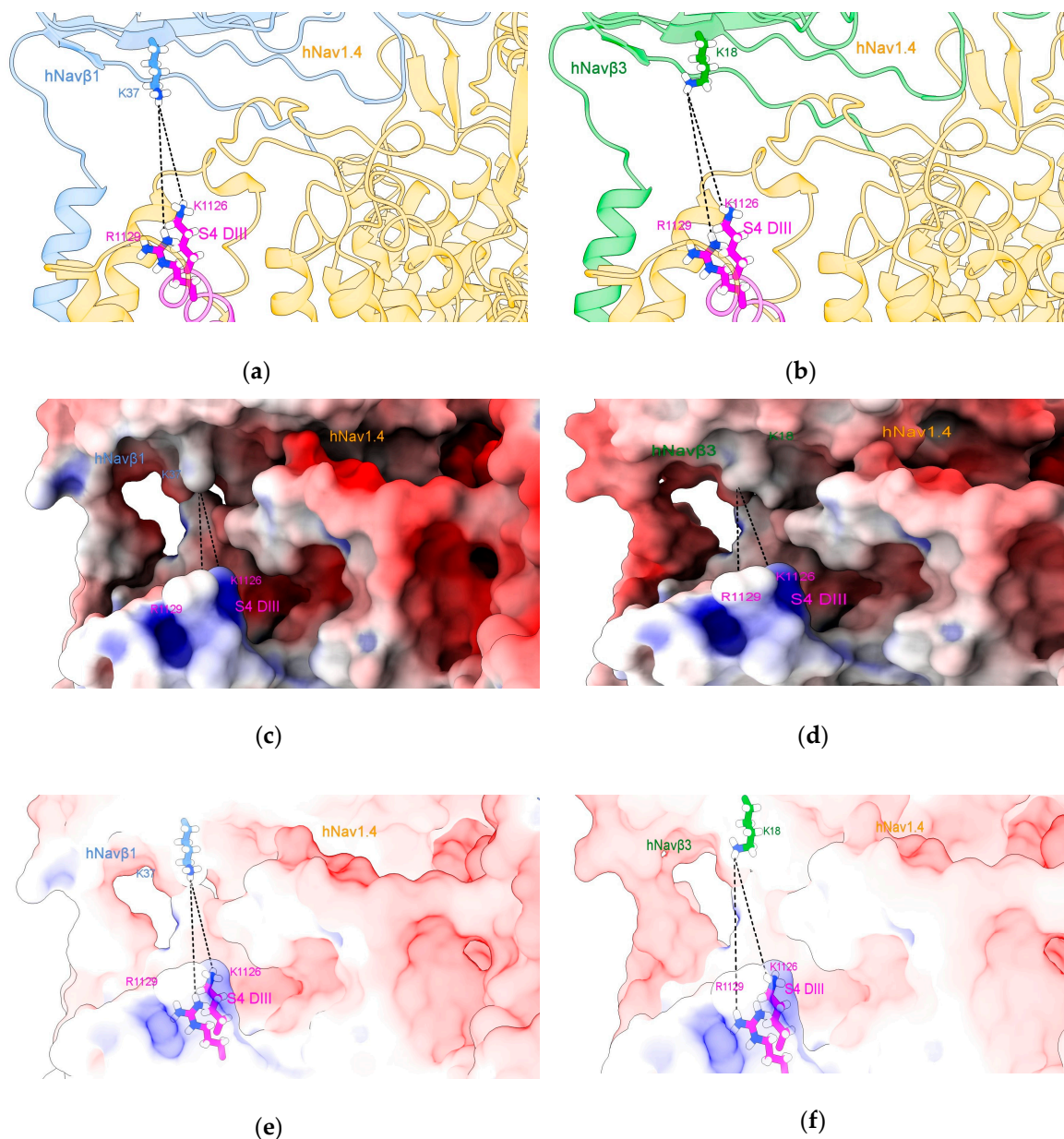


Figure 5. S4 DIII voltage sensor of $\text{hNav}_{1.4}\alpha$ [49] in close contact with $\text{hNav}_{\beta 1}$ [49] or $\text{hNav}_{\beta 3}$ [55]. (a) $\text{hNav}_{1.4}\alpha$ interfaced with $\text{hNav}_{\beta 1}$; (b) $\text{hNav}_{1.4}\alpha$ interfaced with $\text{Na}_v\beta 3$; (c,e) the MEPS at the interface $\text{hNav}_{1.4}\alpha/\text{hNav}_{\beta 1}$; (d,f) the MEPS at the interface between $\text{hNav}_{1.4}\alpha$ and $\text{hNav}_{\beta 3}$. The structures were prepared with Chimera add-on PDB2PQR [63] and MEPS calculated for PPI surfaces using the Adaptive Poisson-Boltzmann Solver (APBS) [64], a plug-in tool in Chimera Alpha 1.14 [61] and simulated under Chimera X [65]. S4 DIII voltage sensor: magenta; $\text{hNav}_{\beta 1}$: cornflower blue; $\text{hNav}_{\beta 3}$: green.

An electrostatic repulsion could be created with the $\text{Na}_v\beta 1$ or $\text{Na}_v\beta 3$ subunits. As a suggested mechanistic consequence, the IF-ECLs move and pull the ECR, which in turn transfers strain energy

onto the $\text{Na}_v\alpha$ subunit. This happens precisely on S4 (DI and DIV) and could generate a conformational change in the channel that accelerates fast inactivation and finally closes the modulation cycle with S4 on DI and DIV returning to its starting positions.

Based on the present findings we propose a possible mechanism of α (pore) modulation by β subunits for the fast inactivation cycle (Figure 6). The acceleration of fast inactivation by the $\text{Na}_v\beta 1$ or $\text{Na}_v\beta 3$. In the PPI model, a rotamer library was applied to find favorable Van der Waals contacts [59–61] concerning $\text{Na}_v\alpha/\text{Na}_v\beta 1$ and $\text{Na}_v\alpha/\text{Na}_v\beta 3$ (Table S1).

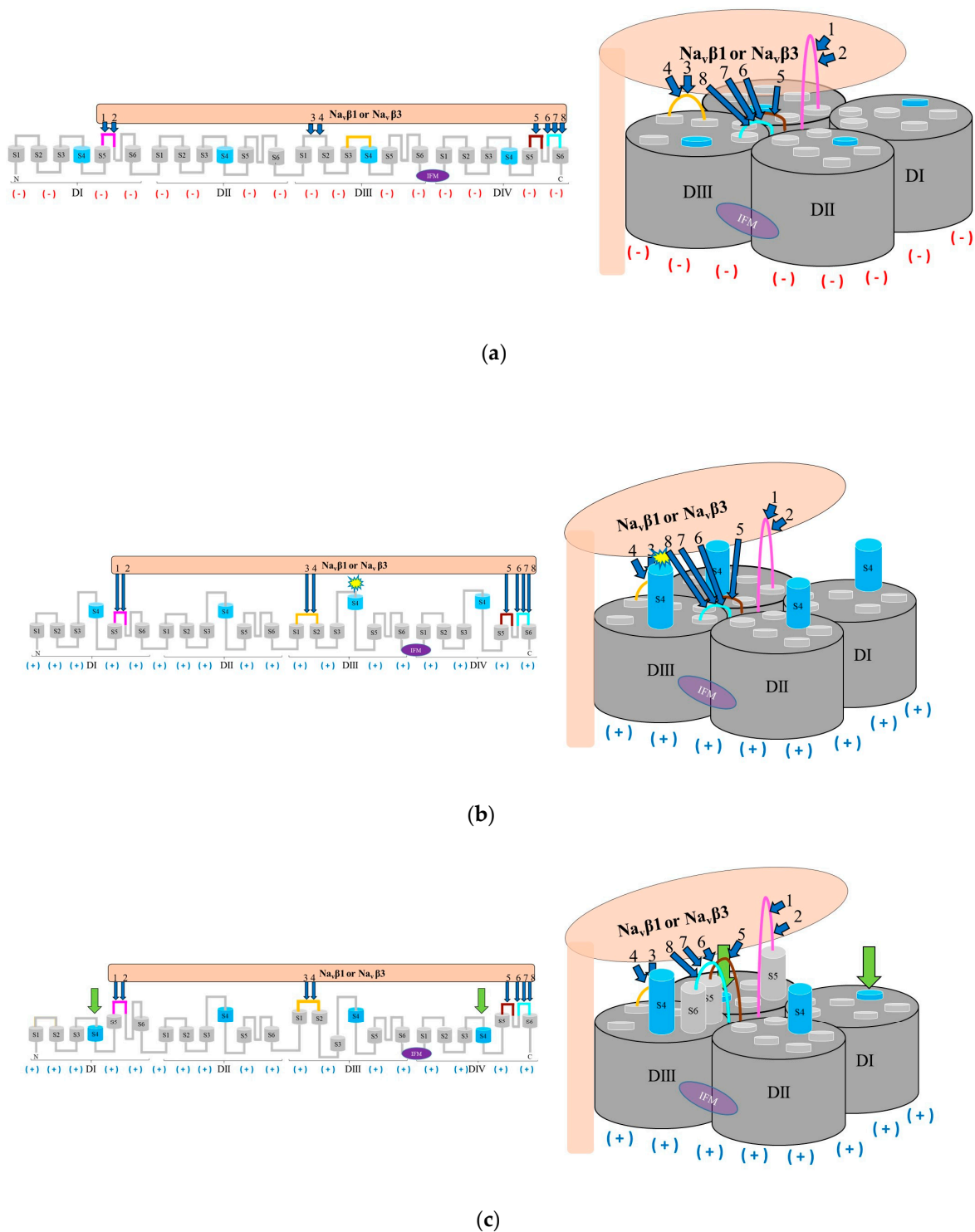


Figure 6. Cont.

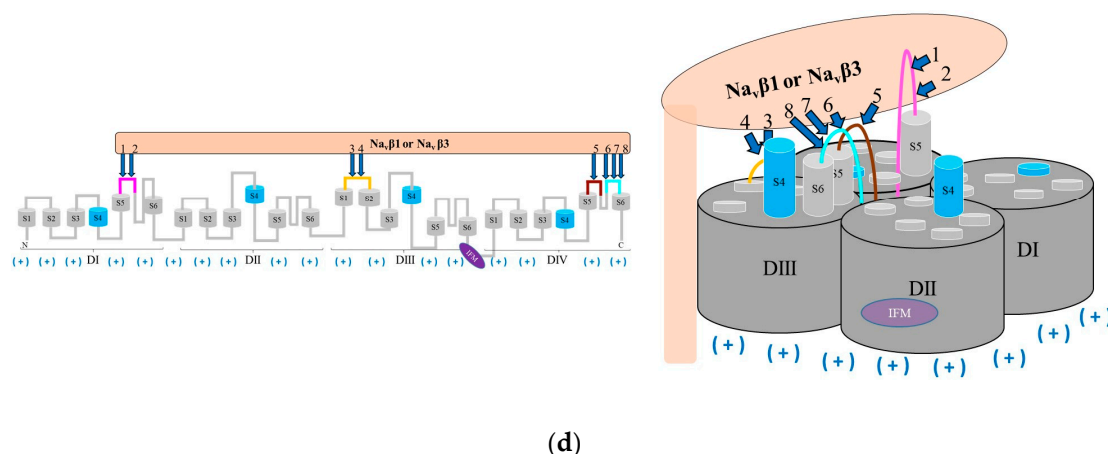


Figure 6. Hypothetical modulation of fast inactivation of $\text{Na}_v\alpha$ gating by $\text{Na}_v\beta1$ or $\text{Na}_v\beta3$; (a) $\text{Na}_v\alpha$ in idle (closed) state in response to interacting $\text{Na}_v\beta1$ or $\text{Na}_v\beta3$; (b) $\text{Na}_v\alpha$ in open (activated) state in presence of $\text{Na}_v\beta1$ or $\text{Na}_v\beta3$ modulation; (c) fast inactivation modulated by $\text{Na}_v\beta1$ or $\text{Na}_v\beta3$; (d) fast inactivation triggered by the IFM inactivation gate; labels 1 to 8: Id of computed polar PPIs (Table S1); computed polar PPIs: navy blue arrows; return to its start position of S4 is forced by IF-ECLs by computed polar interactions with $\text{Na}_v\beta1$ or $\text{Na}_v\beta3$: green arrows; negative charges: red minus signs in parentheses; positive charges: navy blue plus signs in parentheses; $\text{Na}_v\alpha$ regions without PPI: dark and light gray; $\text{Na}_v\beta1$ or $\text{Na}_v\beta3$ subunit: light salmon; S5 DI: magenta; S1-S2 DIII: orange; S5 DIV: brown; S6 DIV: cyan; S4: sky blue, segments S1, S2, S3, S4, S5, and S6: light gray.

2.3. Determination of Relevant ECL Properties

We quantified all ECL sizes from the nine isoforms for the three species (Figure S10), the ECR properties and those for S5 and S6 ECLs (Figure S11), as well as the ECL properties on the α subunit (Figure S12) [66]. Each isoform and ECL presented inherent characteristics, which were discussed in more detail in Section 3.3.

Moreover, the volume and the solvent-accessible area (SAA)—surface area accessible to solvent—were calculated for each ECL of each isoform (Figures S13–S15) [61].

The polar surface area (PSA), nonpolar surface area (NPSA) and MEPS (negative potential: N-MEPS and positive potential: P-MEPS) were measured for the entire IF-ECL as a grand total and the individual values for each IF-ECL (Figures S16 and S17) [61,63,64].

The IF areas of the atoms were determined (Figure S18) besides the buried α and β IF area, i.e., the spatial intersection of IF-ECL with $\text{Na}_v\beta1$ and $\text{Na}_v\beta3$ (Table S3) [61]. To get rid of the loop length bias—longer loops tend to possess more chances of interacting residues than shorter loops—we decided to present normalized values, as a general rule: here we took the IF percentage of aforementioned grand total as the 100% basis. The following properties for IF-ECLs with both β subunits were computed: PSA, NPSA, P-MEPS and N-MEPS. In the next step, common traits (similarities) were detected and clustered into the following interaction patterns: S5 DI: ($\text{Na}_v1.1\alpha$ and $\text{Na}_v1.3\alpha$), ($\text{Na}_v1.5\alpha$ and $\text{Na}_v1.7\alpha$), ($\text{Na}_v1.2\alpha$, $\text{Na}_v1.4\alpha$ and $\text{Na}_v1.6\alpha$), ($\text{Na}_v1.8\alpha$) and ($\text{Na}_v1.9\alpha$); S1-S2 DIII: ($\text{Na}_v1.1\alpha$ and $\text{Na}_v1.4\alpha$), ($\text{Na}_v1.3\alpha$ and $\text{Na}_v1.5\alpha$), ($\text{Na}_v1.2\alpha$ and $\text{Na}_v1.6\alpha$), ($\text{Na}_v1.8\alpha$), and ($\text{Na}_v1.9\alpha$); S5 DIV: ($\text{Na}_v1.1\alpha$ and $\text{Na}_v1.5\alpha$), ($\text{Na}_v1.2\alpha$, $\text{Na}_v1.3\alpha$ and $\text{Na}_v1.6\alpha$), ($\text{Na}_v1.4\alpha$ and $\text{Na}_v1.7\alpha$), ($\text{Na}_v1.8\alpha$), and ($\text{Na}_v1.9\alpha$). In the case of S6 DIV, however, no similarities have been found among the nine isoforms (Figures S19–S21). Supplementary Figure S23 illustrates the $\beta1$ subunit interface and its properties in all details.

2.4. PPI Patterns on $\text{Na}_v\alpha$ Isoforms

The underpinning of protein functions in most biological processes constitutes the plethora of atom-to-atom interactions between proteins and other biomolecules (cf. interactome). Predicting

interactions on an atomic level remains one of the most challenging endeavors in structural biology [67–69].

During evolution protein structure is more conserved than its underlying primary sequence, i.e., sequences diverge from a common ancestor but maintain identical or similar functions with little changes due to homologous exchanges at their active sites [70–72]. Residues at the sensitive interfaces become significant for geometry or signaling and therefore tend to be conserved in the protein structure [73]. Another well-characterized property of interfaces refers to the existence of “hot spot” residues, which are the residues that make the largest contributions to complex formation [74]. In our study context, several reports have raised the question about what atomic components exactly protein interfaces are made of in order to improve prediction power for PPIs [75].

In vitro research to gain mechanistic insight into Na_vs at atomic scale has been a daunting task for decades due to its membrane-embedded location and multidomain complexity [6,76]. It is in such situations when chemometric approaches lend insight unraveling hitherto unnoticed atomic patterns.

$\text{Na}_v\beta$ subunits belong to the immunoglobulin (Ig) superfamily. Its overall structure is an all-beta (strands) fold, which is typical for cell adhesion molecules [77]. Variation in presence (or absence) of β subunits regulates α subunit expression to differentiate tissues. Furthermore, they modulate the pore unit kinetics [78,79] while the mechanism by which this phenomenon occurs has been extensively studied. However, understanding the gating mechanism of the channel and its modulation in details has just emerged in a bitwise manner [80]. Looking back into the channel’s history of research, in 1985 and 2000 respectively, $\text{Na}_v\beta 1$ and $\text{Na}_v\beta 3$ were first reported as cell (surface) adhesion proteins in interaction with the α pore unit through noncovalent bonds [81,82].

New aspects of subunit cooperativity came from A.P. Jackson’s laboratory with Namadurai et al. in 2014 [55] who have elucidated a trimeric crystal structure of $\text{Na}_v\beta 3$, i.e., three IgDs in a crystallographic unit cell. Notwithstanding, it has been an unsettled question if this trimer also reflects a biological unit? Recently, molecular dynamics studies indicated that spontaneous oligomerization of a full-length $\text{Na}_v\beta 3$ subunits to a trimer would probably be a very slow process if it occurred in cell membranes. The three TMH of $\text{Na}_v\beta 3$ would not interact strongly enough [83]. In addition, our team also analyzed whether the IgDs of the $\text{hNa}_v\beta 1$ subunits could form trimers [49]. We determined that in the three IgDs strong repulsion exists between the negative total charges of human Asp25 and Glu27 residues upon fitting them onto the spatial positions of each monomers of the $\text{Na}_v\beta 3$ trimeric structure (PDB: 4L1D [55]). So far, this finding has not been reported elsewhere. Both amino acids have not been exchanged during evaluation across Mammalian species, all of which hints at a pivotal PPI hot spot for $\text{Na}_v\alpha$ subunits (Figure 7, Table S1 and Figures S1–S9). Glass et al. (2020) [83] reasoned that if the $\text{hNa}_v\beta 3$ trimer were to interact with the VSDs of the pore-forming α protein in analogy to structurally known $\text{hNa}_v\beta 1$, a substantial rearrangement of the IgDs would be necessary.

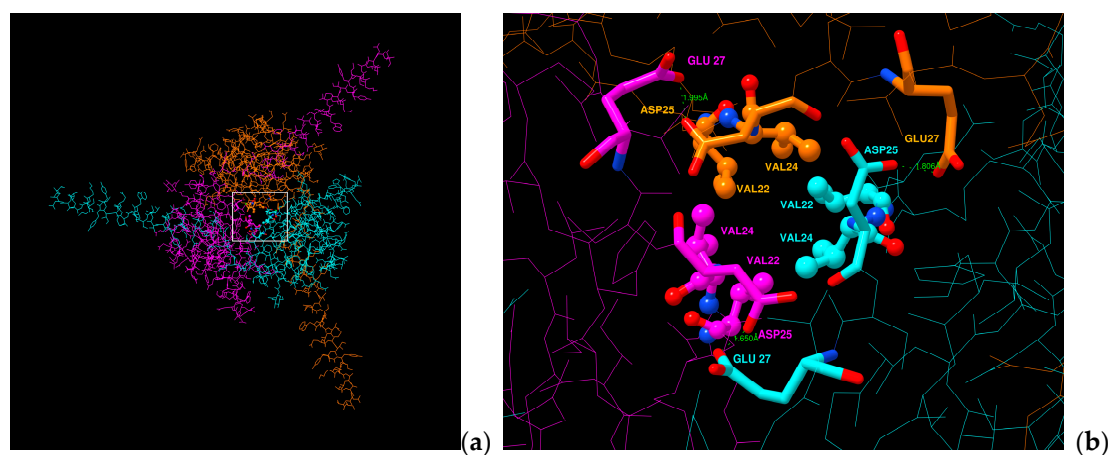


Figure 7. Cont.

Species	
<i>Homo sapiens</i>	GCVEVDSETEAV
<i>Mus musculus</i>	GCVEVDSDEAV
<i>Rattus norvegicus</i>	GCVEVDSETEAV
<i>Bos Taurus</i>	GCVEVDSETEAV
<i>Pan troglodytes</i>	GCVEVDSETEAV
<i>Canis lupus familiaris</i>	GCVEVDSETEAV
<i>Oryctolagus cuniculus</i>	GCVEVDSETEAV
<i>Equus caballus</i>	GCVEVDSETEAV

(c)

Figure 7. Display of a trimeric hNav_vβ1 model. (a) Na_vβ1 trimer seen top-down (b) close-up view from above of the alleged hotspot (c) Aligned sequences from Mammalian species. Negatively charged residues are identical to Asp25 and Glu27 on Na_vβ1 from *Homo sapiens*; white box: analysis area; green dotted lines: computed repulsion of charges; sticks: negative charged residues; sticks and balls: residues that form a possible hydrophobic patch. Data generated by Chimera Alpha 1.14 [61].

Since the crystal structures of α and β1 in complex exist in addition to the trimeric β3 and monomeric β1 (hNavβ3 [55], hNavβ1 [49]) it was possible to carry out structural biology studies by superpositioning them onto each other (Figure 8). Frequently other terms than superpositioning are used: 3D, spatial or structural alignment (SA), in addition to fitting or matching (cf. Magic fit under SPDBV or MatchMaker under Chimera). Here, we used hNav_v1.4α/hNav_vβ1 of the Na_vβ3 trimer [55] and hNav_v1.4α/hNav_vβ1 [49] (Figures 8 and 9).

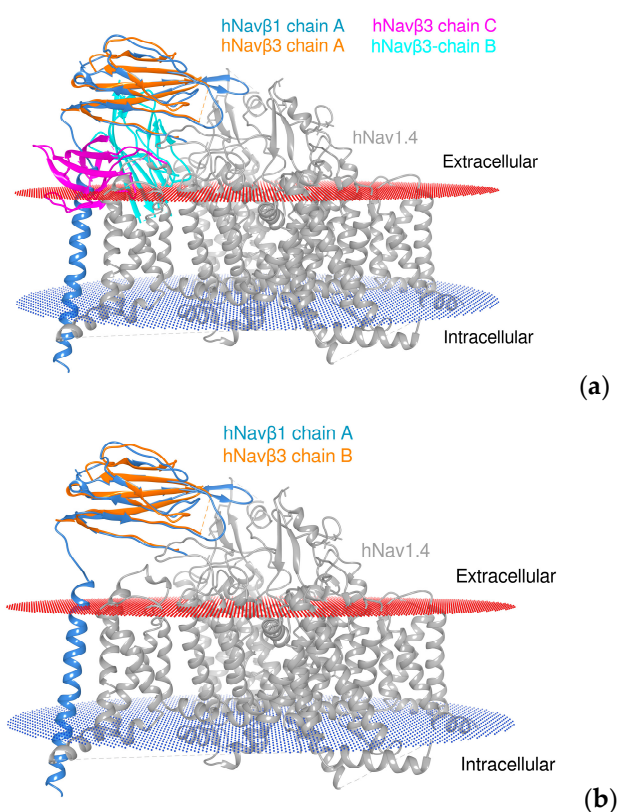


Figure 8. Superposition of monomeric and trimeric 3D models of β proteins. (a) Experimentally determined homotrimeric hNav_vβ3 [55] (three colors: magenta, light blue, beige) in superposition with template hNav_v1.4/hNav_vβ1 (bluish/grey) [49] and (b) one IgD (out of three) subunit(s) of homotrimeric hNav_vβ3 (beige) in superposition with template hNav_v1.4α/hNav_vβ1. It can be seen—by eyesight—that in case a two out of the three subunits bump into the membrane. Extracellular membrane boundaries: dark red; intracellular membrane boundaries: navy blue; Na_vα subunit: gray; hNav_vβ1 subunit: cornflower blue; hNav_vβ3 chains A, B, and C: orange, cyan, and magenta, respectively.

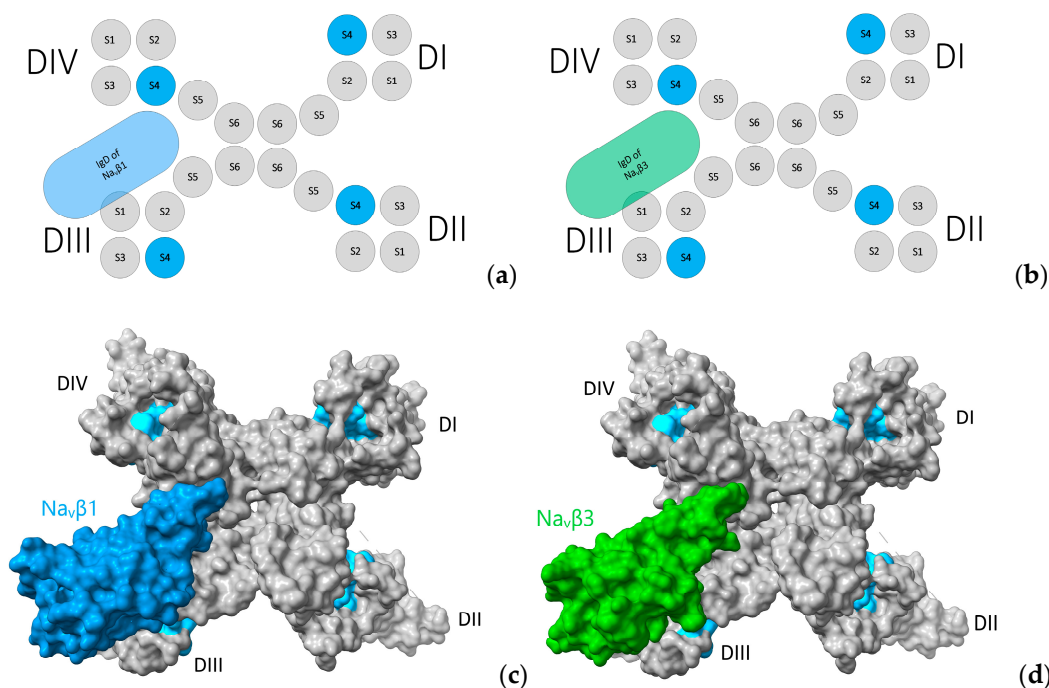


Figure 9. Three-dimensional (3D) location of subunits $\text{Na}_v\beta 1$ and $\text{Na}_v\beta 3$. (a,b) $\text{Na}_v\alpha$ topology in complex with $\text{Na}_v\beta 1$ and $\text{Na}_v\beta 3$. Display of 3D models with solvent-excluded surface areas in panels (c,d). (c) Cryo-EM structure of $\text{hNa}_v\alpha 1.4$ in complex with $\text{Na}_v\beta 1$ [49] and (d) Cryo-EM structures of $\text{hNa}_v\alpha 1.4$ [49] in complex with crystal structure $\text{hNa}_v\beta 3$ [55] positioned according to structural analysis; S4: sky blue; in panels (c,d) the molecular surfaces are colored: $\text{Na}_v\beta 1$: cornflower blue; $\text{Na}_v\beta 3$: green forest; and grey color for $\text{Na}_v\alpha$ subunit surfaces. The same colors were applied to the panels (a,b) above. 3D models by Chimera X [65].

Compared to the sheer number of all-beta fold variations—AKA the Ig superfamily—the ectodomain IgD of $\text{hNa}_v\beta 3$ [55] is extremely similar to IgD of $\text{hNa}_v\beta 1$ [49]. Structural evidence concerning $\text{eeNa}_v 1.4\alpha/\text{eeNa}_v\beta 1$ [48], $\text{hNa}_v 1.4\alpha/\text{hNa}_v\beta 1$ [49], and $\text{hNa}_v 1.7\alpha/\text{hNa}_v\beta 1$ [51] was reported about a binding site in the TM region of $\text{Na}_v\beta 1$ between S1 and S2 helices on VSD DIII [55]. Noteworthy is the finding that the TM regions of the $\text{Na}_v\beta 1$ and $\text{Na}_v\beta 3$ subunits possess high sequence similarity. In vitro studies revealed that the TM region of $\text{Na}_v\beta 3$ non-covalently binds VSD DIII [80] in a way that $\text{Na}_v\beta 1$ does [48,49,51]. Albeit, there is no structural data to pinpoint the location of the $\text{Na}_v\beta 3$ binding site on α subunits.

Frequently, it has been assumed that the $\text{Na}_v\beta 3$ subunit interacts with the $\text{Na}_v\alpha$ subunit through the same mechanism as the $\text{Na}_v\beta 1$ subunit [84]. Nevertheless, in vitro studies demonstrated that both $\text{Na}_v\beta 1$ or $\text{Na}_v\beta 3$ attenuate lidocaine binding to $\text{Na}_v 1.3\alpha$ [85]. Said local anesthetic binds the S6 helix of domain IV by noncovalent bonds [86] and structural evidence affirms that $\text{Na}_v\beta 1$ forms IPP with $\text{Na}_v 1.4\alpha$ in the IF-ECL S6 DIV [48].

As working hypothesis, we proposed that the $\text{Na}_v\beta 3$ binding site on the α pore subunit is the same as that of $\text{Na}_v\beta 1$. The assumption was based on the structural data analyses of 3D aligned $\text{eeNa}_v 1.4\alpha/\text{eeNa}_v\beta 1$ with $\text{hNa}_v 1.4\alpha/\text{hNa}_v\beta 1$. The same conservation pattern is found again in template complex $\text{hNa}_v 1.4\alpha/\text{hNa}_v\beta 3$ in addition to all isoforms across the three species under scrutiny (Table S1 and Figures S1–S9).

In the analyzed (3D) template structures and our 3D models we found interaction patterns at the $\text{Na}_v\alpha/\text{Na}_v\beta 1$ and $\text{Na}_v\alpha/\text{Na}_v\beta 3$ interfaces. Upon inspection, it is safe to generalize our detailed findings that these interaction patterns significantly diverge between isoforms crossing species. In particular, we noted specific PPI patterns between $\text{Na}_v\alpha$ with either $\text{Na}_v\beta 1$ or $\text{Na}_v\beta 3$ subunits.

Applying Chimera's combined two-dimensional (2D) with 3D alignment capacities for rational protein superposition (by MatchMaker), the templates of hNa_vβ1 [49] and hNa_vβ3 [55] were aligned as spatial references (Figure 4b). Thereupon, we identified all interacting residues between template hNa_v1.4α/hNa_vβ1 [49] and 3D model hNa_v1.4α/hNa_vβ3 [49,55] (Figure 3). The identification was assisted by 3D template eeNa_v1.4α/eeNa_vβ1 [48] as a most valuable reference to pinpoint conservation or homology for closely or far-distantly related organisms, here: three Mammalian species versus eel (Figure 2). As an asset for PPI validation, not only sequential but also structural similarities of hNa_vβ3 with hNa_vβ1 lie significantly above the twilight zone of homology with ≈ 50%, RMSD ≈ 1.2, respectively. Taken together all topology patterns, convincing evidence was unveiled by chemometrics, all of which indicate that hNa_vβ3 subunit binds and modulates Na_vα from the same position and via the same mechanism as hNa_vβ1 subunit, because the interacting residue pattern is almost the same (see our 3D model of hNa_v1.4α/Na_vβ3 and PDB entry 6AGF [49] with the hNa_v1.4α/Na_vβ1 in PDB format in SM). Sufficient(ly tiny) variations do exist, however, on both proteins. They could explain to some degree the differences in channel kinetics which has to be confirmed in future studies with more experimental research.

For the sake of inference power of our chemometric output data, we also studied the known structures of hNa_vβ2 [56] and hNa_vβ4 [54]. Again, 2D and 3D alignments were carried out with Chimera against reference structure hNa_vβ1 [49]. All critical data clearly lie in the boundaries of the twilight zone with ≈ 18.8 or 18.1%, RMSD: 4.52 or 7.12, respectively. With hNa_vβ1 [49], hNa_vβ2 [56] (Figure 4c) and hNa_vβ4 [54] (Figure 4d) aligned, the degree of positional mismatches of equivalent residues becomes obvious by eyesight, concerning β2 or β4 sequences vs known interacting residues of reference hNa_vβ1 [49]. The loss of conserved positions for the interacting residues of both subunits (β2, β4) strongly hints at the existence of a totally distinct PPI with the α pore subunit. This finding has not been reported in the literature.

At that stage we can characterize the more general topological behavior of all nine isoforms and lump them together in view of their distinct interaction patterns: (i) isoforms hNa_v, mNa_v and rNa_v (1.2, 1.4 and 1.6), present eight PPIs with Na_vβ1 or Na_vβ3 subunits; (ii) isoforms hNa_v, mNa_v and rNa_v (1.1, 1.3 and 1.7) present seven PPIs. Both share essential features, so we suggest they have a common effect on modulation. In (weak) contrast, isoforms hNa_v, mNa_v, and rNa_v (1.1, 1.3, 1.5, 1.7, 1.8, and 1.9) coincide in a non-interacting residue at position 6 in ECL S6 DIV. In stark contrast, isoforms hNa_v, mNa_v, and rNa_v (1.5, 1.8, and 1.9) always share two features: first, they all lack two or more PPIs and secondly, they all belong to binding type TTX-R, and they associate to an interaction reduction (PPI-Id in Table 1) on S1-S2 DIII ECL, while isoforms hNa_v, mNa_v, and rNa_v (1.9) do not at all interact through S6 DIV ECL. Wrapping up the findings into a mechanistic picture, gating of all those isoforms belonging to binding type TTX-R might also coincide in a common modulation mechanism. The absence of interaction in PPI-Id 6 in ECL S6 DIV concerns the following isoform: h, m, rNa_v (1.1, 1.3, 1.5, 1.7, 1.8, and 1.9). This interaction site (PPI-Id 6) exposes a strong salt bridge for isoforms h, m, rNa_v 1.2, 1.4, and 1.6. (Figures S1–S9). We infer that the presence or absence of that strong electrostatic signal at the IF could be a significant feature to trigger isoform-dependent variations in pore modulation.

3. Discussion

3.1. Hypothetical Acceleration of Fast Inactivation of Gating of the Na_vs

Cell membrane depolarization is associated with an upwards movement to expose the helical S4 voltage sensors into the cell membrane surface (Figure 6). S4 exposition to the surface implies a conformational change of the channel to enter an open state [19–22]. As a topological result, the three-amino acid inactivation gate (IFM) located between helices S6 DIII and S1 DIV swiftly connects to the pore and prevents sodium ions to enter (Na⁺ influx), all of which leads to an inactivated state. Thanks to the identification of interacting residues based on our systematic topological (sequential)

and structural (spatial) models it is possible to link them to reported electrophysiological aspects about functional transition from activation to inactivation of all nine Na_v isoforms (Figure 1) [26,27]. Of note, the variable N-linked glycosylation of the ectodomains (IgDs) does not affect our cheminformatic results because it does not belong to the interface between both subunits [84].

Zhu et al. (2017) [80] concluded from their *in vitro* studies that $\text{Na}_v\beta 1$ and $\text{Na}_v\beta 3$ accelerate the deactivation of S4 in $\text{Na}_v 1.5$, in addition to $\text{Na}_v\beta 1$ in S4 (DIII and DIV) or $\text{Na}_v\beta 3$ in S4 (DIII), respectively. In good keeping, Ferrera et al. (2006) [87] demonstrated that $\text{Na}_v\beta 1$ determines the electrical environment of the channel by changing the surface charges that electrostatically affected the activation of the channels.

In our modeled complexes $\text{Na}_v\alpha/\text{Na}_v\beta 1$ and $\text{Na}_v\alpha/\text{Na}_v\beta 3$ (Table S1 and Figures S1–S10), both β subunits are located in proximity to the S4 voltage sensor on DIII. In hypothetical terms, when the cell membrane is depolarized, S4 on DIII shifts in space and subsequently two conserved positively charged residues on S4 on DIII enter into repulsive contacts with a conserved lysine on both β subunits (Table S2). All three positive charges are clearly exposed on the solvent-accessible area on the protein surface (Figure 5). It is safe to conclude that a strong biochemical signal is triggered when this charge repulsion takes place at S4 DIII (Figure 8). As a direct consequence for the channel's overall geometry, domain shift of IgDs (the ectodomains of $\text{Na}_v\beta 1$ and $\text{Na}_v\beta 3$) takes place to modulate fast inactivation mechanism. The segment S1–S2 on DIII serves as a flexible hinge to form a noncovalent association with $\beta 1$ and $\beta 3$ IgDs. In a slower response to depolarization, S5 on DI and S5 on DIV terminate the cycle by forcing S4 (DI and DIV) back into its initial position in a spring-like fashion. Finally, S6 on DIV arrests—like an anchor—both β subunits. On theoretical ground, the present findings explain the cooperativity between ECRs and certain $\text{Na}_v\beta$ subunits for channel pore modulation. From an evolutionary point-of-view, this makes sense, since calling-in external proteins (auxiliary β s) to assist the protein function (α pore) is achieved much faster than the adaption of loop segments by slow selection of random point mutations over time. Obviously, this happened at a time during cellular evolution when gene fusion already took place to transform the homotetrameric (bacterial) channel into a single chain pore protein, which is composed of four different domains (“monocadear hetero-tetra-domain subunit”). In this context the existence of nine closely related mutants (isoforms) show the work of evolution from the near-past to present time when a common ancestral protein has been evolving along with differential gene expression and tissue specialization.

3.2. Properties of the ECL Residues for $\text{Na}_v\alpha$ Subunits

The ECL sequence lengths are shown in Figure S10. Intriguingly, S5 on DI constitutes the longest ECL. Its aberrant size reflects that it encompasses a second PPI; PPI-Id 1 is conserved in every isoform and species; PPI-Id 2 is conserved in almost all isoforms with the exception of $\text{Na}_v 1.8\alpha$ and $\text{Na}_v 1.9\alpha$. The ECL length of S5 on DIV contains a negatively charged residue (Id 5) which is conserved throughout all nine isoforms for all three species. Possibly, the ECLs of S5 on DI and DIV have evolved steadily in contact with $\text{Na}_v\beta 1$ and $\text{Na}_v\beta 3$ subunits, leading to speculations about their role as main binding sites for $\text{Na}_v\alpha$ modulation.

The chemometric properties describing S5 and S6 are documented in Figure S11. In all three species $\text{Na}_v 1.4\alpha$ (resp. $\text{Na}_v 1.5\alpha$ isoform) accounts for the highest (respectively, lowest) amount of polar and negatively charged residues on S5 and S6. Two isoforms contain the least number of nonpolar residues, namely $\text{Na}_v 1.8\alpha$ and $\text{Na}_v 1.9\alpha$. Both show the highest percentage of polar ECR residues and in particular on ECL S5 and S6 for all three species. Our finding here reflects the extant literature speculating about the absence of experimental evidence for $\text{Na}_v 1.9\alpha$ cooperation with β subunits for gating. Figure S12 summarizes the ECL properties. $\text{Na}_v 1.4\alpha$ and $\text{Na}_v 1.6\alpha$ possess the same number of PPIs. Despite this common trait, subtle differences may also explain why their kinetic behavior differs. The ECL of S5 on DI in $\text{Na}_v 1.4\alpha$ (resp. $\text{Na}_v 1.6\alpha$) hosts the highest (resp. smallest) amount of polar and negatively charged amino acids. Intriguingly, the $\text{Na}_v 1.6\alpha$ isoform accumulates even more polar and negatively charged residues in its S5 loops on DIII. Domains DI and DIII are facing each other

from diametrically opposing positions across the central pore part. Both have developed the longest S5 ECLs among all $\text{Na}_v\alpha$. It can be speculated that their lengths could reflect the main electrostatic attraction of the $\text{Na}_v\alpha$ for the conduction of Na^+ towards the channel pore. This balance of residues distributed in the S5 ECLs (DI and DIII) probably has evolved to provide the $\text{Na}_v1.4\alpha$ and $\text{Na}_v1.6\alpha$ isoforms a MEPS similar to a fingerprint with inherent characteristics to perform a specific function on the tissue. Aforementioned findings have not been reported in the extant literature that far.

3.3. Volume and Surface Properties of the ECL on $\text{Na}_v\alpha$ Subunits

Evolution leads to random point mutations or SNPs with variable consequences for survival of organisms. On molecular level it changes structures and functions [88,89]. Isoforms can be understood as transient states during divergent evolution to separate them from a common ancestral protein when cells evolve to more specialized tissues in organisms [90,91]. Biochemical signaling is not seldom located on exposed loop segments on cell surfaces with a remarkable conservation of signal-relevant residues amidst the variable loop segments. This observation is the rationale to combine 2D and 3D alignment techniques enabling us to reveal this hidden world of signaling or interacting amino acids at the α/β interface [92–94]. The type of protein structure—AKA fold unit—is more conserved than its underlying primary sequence. Moreover, unchanged structures keep the biochemical function, what sometimes can be observed even in extreme cases of sequence divergence [95–97]. Of note, each ECR has 16 ECLs on each isoform.

With respect to all nine isoforms, the $\text{Na}_v1.4\alpha$ isoform has the largest volume and widest SAA concerning the ECR in general. Moreover, regarding the pore architecture, this holds true also for S5 and S6 of ECLs. In contrast, the $\text{Na}_v1.9\alpha$ isoform it has the smallest volume and SAA in the ECR and ECLs S5 and S6 (Figure S13). This finding has not yet been reported by others.

Figures S14 and S15, respectively, display the molecular volume and SAA of the ECLs. The S5 DI ECLs on h, m, $\text{rNa}_v1.4\alpha$ have a fairly larger molecular volume than the other isoforms. In contrast, the molecular volume of the S6 DIV ECLs on $\text{Na}_v1.9\alpha$ is significantly smaller than on all other isoforms. This finding nicely explains why $\text{Na}_v1.9\alpha$ isoforms do not enter in contact both β subunits via ECL S6 DIV and has not yet been reported by others either.

Of all isoforms, the h, m, $\text{rNa}_v1.4\alpha$ (h, m, $\text{rNa}_v1.8\alpha$ and h, m, $\text{rNa}_v1.9\alpha$) isoforms have the highest N-MEPS (P-MEPS) in the IF-ECLs (Figure S16). These patterns are identical for S5 DI and S6 DIV ECLs. On the other hand, $\text{Na}_v1.8\alpha$ and $\text{Na}_v1.9\alpha$ have higher P-MEPS for S1-S2 DIII ECLs. Intriguingly, $\text{Na}_v1.4$ isoforms possess the smallest areas of N-MEPs in S1-S2 DIII ECLs (Figure S17). The isoform-dependent characteristic features of each isoform could be attributed to the affinity of electrostatic attraction to the $\text{Na}_v\beta1$ and $\text{Na}_v\beta3$ subunits.

3.4. Interface Properties Between $\text{Na}_v\alpha$ and $\text{Na}_v\beta1$ or $\text{Na}_v\beta3$

The observation that only a tiny portion of the total surface area belongs to structural or functional segments is reflected by high conservation at those segments [98–101]. Especially electrostatic forces often act as critical determinants for biochemical signaling or other protein functions like ligand recognition, affinities, or structural stability. PPI is said to take place at surface locations (patches) with geometric and chemical complementarity [101–105]. This way, ECLs on the sodium channel tend to keep physicochemical similarities on their surfaces all of which sum up into distinct interaction patterns.

The variable surface area between the IF-ECLs and both β subunits was documented in Figure S18. For most of the Na_v s isoforms, the following general interaction pattern holds in order of shrinking surface: S5 DI > S1–S2 DIII > S6 DIV > S5 DIV, with the exception of $\text{Na}_v1.9$ isoforms, where the interface area of the IF-ECL S6 DIV and the $\text{Na}_v\beta1$ and $\text{Na}_v\beta3$ subunits was found to be much smaller compared to all other isoforms. The observation is in excellent keeping with the electrophysiological role of h, m, $\text{rNa}_v1.9\alpha$, lacking PPI with both β subunits. Hence, it seems not far-fetched to infer that it does not interact with IF-ECL S6 DIV.

Figures S19–S22 inform about the percentage scores concerning IF-ECLs and both β subunits for the following properties: PSA, NPSA, P-MEPS, and N-MEPS, measured on an atomic scale, which only counts the PPI atoms (Figure S18). The isoforms $\text{Na}_v1.2$ and $\text{Na}_v1.6$ possess interaction patterns, which resemble those of the IF-ECLs S5 DI, S1-S2 DIII, and S5 DIV. Our finding here could explain why the interface surface properties in both subunits ($\text{Na}_v\alpha$ and $\text{Na}_v\beta$) are conserved because they reflect similar modulation. Interestingly, $\text{Na}_v1.2\alpha$ and $\text{Na}_v1.6\alpha$ present the same PPI sites along with $\text{Na}_v1.4\alpha$. Yet, the size, residue properties, SAA, molecular volume, differ greatly between either $\text{Na}_v1.2\alpha$ or $\text{Na}_v1.6\alpha$ versus $\text{Na}_v1.4\alpha$, emphasizing the IF-ECLs on S5 DI. On the other hand, IF-ECLs on S6 DIV do not show any similarity between isoforms, all of which is in line with the pivotal role of IF-ECLs S6 DIV as a strong contributor to pore modulation because of its unique electrostatic forces on its surface.

4. Materials and Methods

4.1. In Silico Homology Modeling

Homology modeling techniques were carried out to generate (3D) structure models of the hitherto unknown β subunits of mice and rats ($\text{mNa}_v\beta1$, $\text{mNa}_v\beta3$, $\text{rNa}_v\beta1$, and $\text{rNa}_v\beta3$) as well as the isoforms of the following $\text{Na}_v\alpha/\text{Na}_v\beta$ complexes: $\text{hNa}_v1.1\alpha$, $\text{hNa}_v1.3\alpha$, $\text{hNa}_v1.6\alpha$, $\text{hNa}_v1.8\alpha$, $\text{hNa}_v1.9\alpha$, $\text{mNa}_v1.1\alpha$ to $\text{mNa}_v1.9\alpha$, $\text{rNa}_v1.1\alpha$ to $\text{rNa}_v1.4\alpha$, $\text{rNa}_v1.6\alpha$ to $\text{rNa}_v1.9\alpha$. Two programs, MODELLER 9.22 [106] and Chimera alpha V.1.14 [61], were applied using the following cryo-EM as (3D) templates: $\text{hNa}_v1.4\alpha/\text{hNa}_v\beta1$ with chains A and B from PDB entry 6AGF [49], $\text{hNa}_v1.2\alpha$ with chain A from PDB entry 6J8E [50], $\text{hNa}_v1.7\alpha$ with chain A, from PDB entry 6J8G [51], $\text{rNa}_v1.5\alpha$ from PDB entry 6UZ0 [52]. The following crystal structures were also taken as templates: $\text{hNa}_v\beta2$ from PDB entry 5FEB [56], $\text{hNa}_v\beta3$ with chain A from PDB entry 4L1D [55], and finally $\text{hNa}_v\beta4$ from PDB entry 4MZ2 [54].

4.2. Identification of Interacting Residues at the Interface Between $\text{Na}_v\alpha$ and $\text{Na}_v\beta$

The advent of a complete sodium channel structure with pore part and auxiliary proteins from a higher (vertebrate) organism has ushered a new area of structural biology analysis to lend insight into the underpinnings of subunit modulation mechanisms. The structure elucidation was a pivotal step because vertebrate Na_v channels are composed of a monomeric (single-chain) α protein with four different domains (I to IV), in contrast to the hitherto known homo-tetrameric (4 chains) channels of bacterial species without auxiliary proteins. Precisely, our cheminformatic work exploits this first experimentally observed interface of $\text{Na}_v1.4\alpha$ isoform complex from a vertebrate species: the eel ($\text{eeNa}_v\alpha/\text{Na}_v\beta$ for short, PDB entry: 6AGF [48]). This template helped analyze the interacting amino acids which form the PPI in the ECR (here: $\text{eeNa}_v\alpha/\text{Na}_v\beta$) applying software tools to detect contacts at the interface and the databases of Dunbrack and Dynaomics rotamers [59,60]. MSA was always performed using web based Clustal Omega 1.2.4 under its default settings [62]. To get rid of the residue numbering problems in sight of variable sequence lengths, each identified residue as “interacting” (i.e., forming the PPI of $\text{eeNa}_v1.4\alpha/\text{eeNa}_v\beta1$ [48]) was labelled as a small segment of seven adjacent amino acids. In its central position, the interacting residue is flanked by three amino acids on either side. The schematic pattern is “yyyXyyy”, where “y” symbolizes any amino acid, while “X” is the interacting amino acid.

4.3. The Input Structures as Templates for the PPI Models

To generate the interfaces the following templates were used: the cryo-EM structure of $\text{hNa}_v\beta1$ from PDB entry 6AGF [49], chain A of $\text{hNa}_v\beta3$ crystal structure from PDB entry 4L1D [55]. Moreover, the following homology models were generated for the $\text{mNa}_v\beta1$ subunits, $\text{mNa}_v\beta3$, $\text{rNa}_v\beta1$, and $\text{rNa}_v\beta3$, in addition to the computed isoform complexes $\text{hNa}_v1.1\alpha$, $\text{hNa}_v1.3\alpha$, $\text{hNa}_v1.5\alpha$, $\text{hNa}_v1.6\alpha$, $\text{hNa}_v1.8\alpha$, $\text{hNa}_v1.9\alpha$, $\text{mNa}_v1.1\alpha$ to $\text{mNa}_v1.9\alpha$, $\text{rNa}_v1.1\alpha$ to $\text{rNa}_v1.4\alpha$, $\text{rNa}_v1.6\alpha$ to $\text{rNa}_v1.9\alpha$. We also used the cryo-EM structures of $\text{hNa}_v1.4\alpha$ isoform with chains A and B from PDB entry 6AGF [49]),

hNa_v1.2 α with chain A from PDB entry 6J8E [50]), hNa_v1.7 α with chain A from PDB 6J8G [51]), rNa_v1.5 α from PDB entry 6UZ0 [52]). Of note, no chimeric combinations were made crossing species.

4.4. Determination of the Extracellular Regions of all Na_v α Subunits

The structures and sequences of the ECLs of the isoforms hNa_v1.1 α to hNa_v1.9 α , mNa_v1.1 α to mNa_v1.9 α and rNa_v1.1 α to rNa_v1.9 α , were determined, based on the available template structures eeNa_v1.4 α , hNa_v1.2 α , hNa_v1.4 α , rNa_v1.5 α and hNa_v1.7 α which had been downloaded from the Orientations of Proteins in Membranes (OPM) database [107]. OPM provides spatial information about the lipid bilayer packing of the transmembrane helical part for our channel models. OPM helped define the ECR, i.e., at which position the loop protrudes and re-enters TMH.

4.5. Calculation of the Properties for all ECLs

The 432 amino acid segments, which define all ECLs under scrutiny were computed, i.e., D1 to DIV with 4 ectodomain loops, and each of them by nine isoforms for three species yield $16 \times 9 \times 3 = 432$ topological models. They were “extracted” from the primary sequences of hNa_v1.1 α to hNa_v1.9 α , mNa_v1.1 α to mNa_v1.9 α and rNa_v1.1 α to rNa_v1.9 α . The ECL lengths and informative properties about the interacting amino acids were systematically computed and documented for subsequent PPI analyses. The plethora of data made scripting a most valuable asset under Chimera (see scripts at the end of SM). Chemometric properties—AKA descriptors or parameters—included polar and nonpolar area, cysteines, or aromatic amino acids. Of note, hydrogen bonding was observed and documented, but data presentation omitted, since constructing the intra- or intermolecular hydrogen networking is a standard option. The H-bonds at interfaces are readily on display, i.e., intermolecular hydrogen networks (in the contact zone, which is defined by an atom selection radius) between two proteins (see our 3D model of hNa_v1.4 α /Na_v β 3 and PDB entry 6AGF [49] with the hNa_v1.4 α /Na_v β 1 in PDB format in SM).

4.6. Calculation of the Chemical Surface Properties for All IF-ECLs

For all 3D models the potential energies of the structures were minimized and total and partial charges loaded with a water probe radius of 1.4 Å and a vertex density of 2.0 [108]. The molecular volume, total SAA as well as the polar or non-polar SAA of charged or uncharged atoms were estimated in Å² for all ECLs [61]. As usual all data was computed for all nine isoforms of the three species.

4.7. Electrostatic Interactions of the IF-ECLs Surfaces (MEPS)

Structural input files (models and 3D templates) were prepared with Chimera add-on PDB2PQR, according to a protocol [63]. It computes Poisson-Boltzmann electrostatics, which constitutes a higher level of theory than electrostatic forces calculated based on Poisson-Boltzmann equation solver (APBS) [64]. The numerical output was converted for graphical display of MEPS. To this end, all those data points above and below a given threshold (± 30) were excluded (empiric protocol). Electrostatic force values in the +30 to −30 range were considered for linear scaling the color code between +1 and −1 (unit one data normalization). The corresponding load at each vertex of the surface was assigned using the UCSF Chimera alpha V. 1.14 interface [61] in molecular selections for each ECL.

4.8. Calculation of the ECL Surface Properties at the Interface with Na_v β 1 and Na_v β 3 Subunits

At the interface the buried area, total SAA and polar and non-polar areas were calculated in Å² applying scripts under Chimera [61]. For direct comparison some values were expressed as percentages to reflect the relative portion (%) of the total loop length (100 %) to account for the huge variation in length. In addition, residues with positive or negative charges were taken as basis to compare MEPS at the interface.

4.9. External Model Validation of the PPI Models

In a more general view, the advent of structural knowledge about the cell proteome has ushered a new area of PPI studies identifying hotspots of interaction between adjacent proteins [109]. After finishing our study, a fully automated interface generation was carried out. The web-based tool identified the same interacting residues (see final section of the Supplementary Materials [110]).

5. Conclusions

In this work, we analyzed observed protein-protein interfaces and postulated others in models derived from experimentally determined 3D templates. The models were generated for all nine existing isoforms of three species (human, rat, mouse). The interface concerned the residues of extracellular loops in close contact with the $\text{Na}_v\beta 1$ or $\text{Na}_v\beta 3$ subunits. Thanks to the chemometric analysis, we formulated a model for fast inactivation of the $\text{Na}_v\alpha$ pore gating modulated by the presence of either $\text{Na}_v\beta 1$ or $\text{Na}_v\beta 3$ auxiliary proteins. On theoretical ground, we gained mechanistic insight of the movements around the S4 DIII voltage sensor, which is modulated by β subunits.

We describe the modulation of the sodium channel activity in terms of a schematic PPI model between pore-containing transmembrane α protein and the auxiliary β proteins for all nine isoforms in three Mammalian species. Our structural models and topological analysis of sequences lead to the conclusion that their distinct interfaces reflect the observed differences in gating kinetics.

We computed chemometric patterns for criteria like non-covalent bonding, loop length, area or volume, solvent accessible area or buried surfaces and other electrostatic descriptors. Isoforms were grouped together according to common interaction patterns and opposed to others with different patterns, and all results were mechanistically related to reports on gating kinetics. The patterns included solvent accessible area or conserved positions for oppositely charged residues on either side of the interface. Our findings about subtle variations in the electrostatic patterns affect the individual modulation capacity of each isoform all of which is in keeping with electrophysiologic observations of gating kinetics and graphically resumed in our schematic drawings.

Our cheminformatic study was thoroughly based on observations taken from the extant literature, and our results are in line with their experimental findings. In addition, we report two hitherto unidentified interaction patterns (or patches) for the 3D templates as well as the proposed interface models. They fit into a larger mechanistic picture with the other interaction patches, which were first reported by Yan et al. with the advent of a complete sodium channel structure for vertebrate species (eel) [48].

This work could orient future research in molecular biology or help design site-directed mutagenesis studies at the subunit interface of voltage-gated sodium channels. In particular, molecular dynamics studies on supercomputers could simulate the gating trajectories over time and confirm that the isoform movements can be grouped together following the proposed cheminformatic patterns.

Supplementary Materials: The following are available online: **Table S1.** PPI of the residues of the $\text{Nav}\alpha$ and $\text{Nav}\beta$ subunits; **Table S2.** Residues of contact of Navs S4 DIII with the $\text{Nav}\beta 1$ and $\text{Nav}\beta 3$ subunits; **Table S3.** Interface area of the IF-ECLs of the Navs; **Table S4.** The output list of interacting residues between both subunits for the eel sodium channel; **Figure S1.** PPIs of the three h, m, rNav1.1 isoforms in complex with $\text{Nav}\beta 1$ and $\text{Nav}\beta 3$; **Figure S2.** PPIs of the three h, m, rNav1.2 isoforms in complex with $\text{Nav}\beta 1$ and $\text{Nav}\beta 3$; **Figure S3.** PPIs of the three Nav1.3 isoforms in complex with $\text{Nav}\beta 1$ and $\text{Nav}\beta 3$; **Figure S4.** PPIs of the three h, m, rNav1.4 isoforms in complex with $\text{Nav}\beta 1$ and $\text{Nav}\beta 3$; **Figure S5.** PPIs of the three h, m, rNav1.5 isoforms in complex with $\text{Nav}\beta 1$ and $\text{Nav}\beta 3$; **Figure S6.** PPIs of the three h, m, rNav1.6 isoforms in complex with $\text{Nav}\beta 1$ and $\text{Nav}\beta 3$; **Figure S7.** PPIs of the three h, m, rNav1.7 isoforms in complex with $\text{Nav}\beta 1$ and $\text{Nav}\beta 3$; **Figure S8.** PPIs of the three h, m, rNav1.8 isoforms in complex with $\text{Nav}\beta 1$ and $\text{Nav}\beta 3$; **Figure S9.** PPIs of the three h, m, rNav1.9 isoforms in complex with $\text{Nav}\beta 1$ and $\text{Nav}\beta 3$; **Figure S10.** Length of extracellular loops of the Navs; extracellular loops: S1-S2, S3-S4, S5 and S6; **Figure S11.** Properties of the residues of the extracellular region of the Nav; **Figure S12.** Properties of residues of Nav extracellular loops; **Figure S13.** Surface and volume properties of ECR and S5, and S6 extracellular loops; **Figure S14.** SAA of ECLs of the Navs; **Figure S15.** Molecular volume of ECLs of the Navs; **Figure S16.** Properties of total SAA of IF-ECLs of Navs; **Figure S17.** Properties of SAA of IF-ECLs of Nav; **Figure S18.** Total area of the atoms that form at the $\text{Nav}\alpha/\text{Nav}\beta$ interface; **Figure S19.** Percentage scores of the surface properties for atoms at $\text{Nav}\alpha/\text{Nav}\beta$ of ECL on S5 DI; **Figure S20.** Percentage of the surface properties of

atoms that form at the Nav α /Nav β interface of ECL S1-S2 DIII; **Figure S21**. Percentage of the surface properties of atoms that form at the Nav α /Nav β interface of ECL S5 DIV; **Figure S22**. Percentage of the surface properties of atoms that form at the Nav α /Nav β interface of ECL S6 DIV; **Figure S23**. Demonstration example of the surface of atoms that form the interface in hNav β 1 with the ECL S5 DI in the HMSR of hNav β 1/hNav1.4 complex.

Author Contributions: Authorship was limited to those who have contributed substantially to the work reported. F.V.-D., S.L.-N., J.E.R.-C., and T.S. carried out the in silico research and graphical artwork. T.S. and F.V.-D. wrote the article. E.M.S.-S. provided bibliographic and in-house information from his ongoing electrophysiological experiments. Conceptualization by T.S.; methodology by T.S. and F.V.-D.; software by F.V.-D., S.L.-N., J.E.R.-C., and T.S.; in-house validation and formal analyses by E.M.S.-S., a research study by F.V.-D. and T.S.; Lab resources by T.S.; data curation by F.V.-D. and S.L.-N.; writing original Spanish version by F.V.-D.; writing, reviewing, and editing by T.S.; model visualization by F.V.-D., S.L.-N., and J.E.R.-C. and; supervision T.S.; project administration by T.S.; internal funding acquisitions by T.S. and E.M.S.-S. All authors have read and agreed to the published version of the manuscript.

Funding: This research received no external funding.

Acknowledgments: We thank the academic teachers Lourdes Milan, for supervising the PhD work of first author Fernando Villa. We also address our thanks to the Mexican CONACyT and VIEP of BUAP for scholarships and administrative support for Fernando Villa. We feel much beholden for the scientific discussions and advice of Anthony P. Jackson, Department of Biochemistry, University of Cambridge, UK, as well as for the internal funding for experimental work and publication fees by Ygnacio Martinez-Laguna, BUAP/VIEP (project ID: 00115) as well as BUAP-CA-120 (area name: Pharmacology-biology).

Conflicts of Interest: The authors declare no conflict of interest.

References

1. Catterall, W.A.; Goldin, A.L.; Waxman, S.G. International Union of Pharmacology. XLVII. Nomenclature and Structure-Function Relationships of Voltage-Gated Sodium Channels. *Pharmacol. Rev.* **2005**, *57*, 397–409. [[CrossRef](#)] [[PubMed](#)]
2. Fux, J.E.; Mehta, A.; Moffat, J.; Spafford, J.D. Eukaryotic Voltage-Gated Sodium Channels: On Their Origins, Asymmetries, Losses, Diversification and Adaptations. *Front. Physiol.* **2018**, *9*, 9. [[CrossRef](#)] [[PubMed](#)]
3. Waxman, S.G. Sodium channels, the electrogenosome and the electrogenistat: Lessons and questions from the clinic. *J. Physiol.* **2012**, *590*, 2601–2612. [[CrossRef](#)] [[PubMed](#)]
4. Goldin, A.L.; Barchi, R.L.; Caldwell, J.H.; Hofmann, F.; Howe, J.R.; Hunter, J.C.; Kallen, R.G.; Mandel, G.; Meisler, M.H.; Netter, Y.B.; et al. Nomenclature of voltage-gated sodium channels. *Neuron* **2000**, *28*, 365–368. [[CrossRef](#)]
5. O'Malley, H.A.; Isom, L.L. Sodium channel β subunits: Emerging targets in channelopathies. *Annu. Rev. Physiol.* **2015**, *77*, 481–504. [[CrossRef](#)]
6. Catterall, W.A. From Ionic Currents to Molecular Mechanisms. *Neuron* **2000**, *26*, 13–25. [[CrossRef](#)]
7. Ogata, N.; Ohishi, Y. Molecular diversity of structure and function of the voltage-gated Na⁺ channels. *Jpn. J. Pharmacol.* **2002**, *88*, 365–377. [[CrossRef](#)]
8. Woolf, C.J.; Mannion, R.J. Neuropathic pain: Aetiology, symptoms, mechanisms, and management. *Lancet* **1999**, *353*, 1959–1964. [[CrossRef](#)]
9. Catterall, W.A. Sodium Channels, Inherited Epilepsy, and Antiepileptic Drugs. *Annu. Rev. Pharmacol. Toxicol.* **2014**, *54*, 317–338. [[CrossRef](#)]
10. Claes, L.R.; Deprez, L.; Suls, A.; Baets, J.; Smets, K.; Van Dyck, T.; Deconinck, T.; Jordanova, A.; De Jonghe, P. The SCN1A variant database: A novel research and diagnostic tool. *Hum. Mutat.* **2009**, *30*, E904–E920. [[CrossRef](#)]
11. Huang, W.; Liu, M.; Yan, S.; Yan, N. Structure-based assessment of disease-related mutations in human voltage-gated sodium channels. *Protein Cell* **2017**, *8*, 401–438. [[CrossRef](#)] [[PubMed](#)]
12. Rubinstein, M.; Patowary, A.; Stanaway, I.B.; Mccord, E.; Nesbitt, R.R.; Archer, M.; Scheuer, T.; Nickerson, D.; Raskind, W.H.; Wijsman, E.M.; et al. Association of rare missense variants in the second intracellular loop of NaV1.7 sodium channels with familial autism. *Mol. Psychiatry* **2016**, *23*, 231–239. [[CrossRef](#)] [[PubMed](#)]
13. Catterall, W.A.; Cestele, S.; Yarov-Yarovoy, V.; Yu, F.H.; Konoki, K.; Scheuer, T. Voltage-gated ion channels and gating modifier toxins. *Toxicon* **2007**, *49*, 124–141. [[CrossRef](#)] [[PubMed](#)]
14. Bagal, S.K.; E Marron, B.; Owen, R.M.; Storer, R.I.; A Swain, N. Voltage gated sodium channels as drug discovery targets. *Channels* **2015**, *9*, 360–366. [[CrossRef](#)] [[PubMed](#)]

15. Ruiz, M.D.L.; Kraus, R.L. Voltage-Gated Sodium Channels: Structure, Function, Pharmacology, and Clinical Indications. *J. Med. Chem.* **2015**, *58*, 7093–7118. [[CrossRef](#)] [[PubMed](#)]
16. Stevens, M.; Peigneur, S.; Tytgat, J. Neurotoxins and Their Binding Areas on Voltage-Gated Sodium Channels. *Front. Pharmacol.* **2011**, *2*, 71. [[CrossRef](#)] [[PubMed](#)]
17. Mantegazza, M.; Catterall, W.A. *Voltage-Gated Na⁺ Channels*; Oxford University Press (OUP): Oxford, UK, 2012; Volume 80, pp. 41–54.
18. Ahern, C.A.; Payandeh, J.; Bosmans, F.; Chanda, B. The hitchhiker's guide to the voltage-gated sodium channel galaxy. *J. Gen. Physiol.* **2015**, *147*, 1–24. [[CrossRef](#)]
19. Payandeh, J.; Scheuer, T.; Zheng, N.; Catterall, W.A. The crystal structure of a voltage-gated sodium channel. *Nature* **2011**, *475*, 353–358. [[CrossRef](#)]
20. Long, S.B.; Tao, X.; Campbell, E.B.; MacKinnon, R. Atomic structure of a voltage-dependent K⁺ channel in a lipid membrane-like environment. *Nature* **2007**, *450*, 376–382. [[CrossRef](#)]
21. Long, S.B. Crystal Structure of a Mammalian Voltage-Dependent Shaker Family K⁺ Channel. *Science* **2005**, *309*, 897–903. [[CrossRef](#)]
22. Yu, F.H.; Yarov-Yarovoy, V.; Gutman, G.A.; Catterall, W.A. Overview of Molecular Relationships in the Voltage-Gated Ion Channel Superfamily. *Pharmacol. Rev.* **2005**, *57*, 387–395. [[CrossRef](#)] [[PubMed](#)]
23. Chanda, B.; Bezanilla, F. Tracking Voltage-dependent Conformational Changes in Skeletal Muscle Sodium Channel during Activation. *J. Gen. Physiol.* **2002**, *120*, 629–645. [[CrossRef](#)] [[PubMed](#)]
24. Bosmans, F.; Martin-Eauclaire, M.-F.; Swartz, K.J. Deconstructing voltage sensor function and pharmacology in sodium channels. *Nature* **2008**, *456*, 202–208. [[CrossRef](#)] [[PubMed](#)]
25. Capes, D.L.; Goldschen-Ohm, M.P.; Arcisio-Miranda, M.; Bezanilla, F.; Chanda, B. Domain IV voltage-sensor movement is both sufficient and rate limiting for fast inactivation in sodium channels. *J. Gen. Physiol.* **2013**, *142*, 101–112. [[CrossRef](#)] [[PubMed](#)]
26. Catterall, W.A. Voltage-gated sodium channels at 60: Structure, function and pathophysiology. *J. Physiol.* **2012**, *590*, 2577–2589. [[CrossRef](#)]
27. Vargas, E.; Yarov-Yarovoy, V.; Khalili-Araghi, F.; Catterall, W.A.; Klein, M.L.; Tarek, M.; Lindahl, E.; Schulten, K.; Perozo, E.; Bezanilla, F.; et al. An emerging consensus on voltage-dependent gating from computational modeling and molecular dynamics simulations. *J. Gen. Physiol.* **2012**, *140*, 587–594. [[CrossRef](#)]
28. Brackenbury, W.J.; Isom, L.L. Na⁺ Channel? Subunits: Overachievers of the Ion Channel Family. *Front. Pharmacol.* **2011**, *2*, 53. [[CrossRef](#)]
29. Cusdin, F.S.; Clare, J.J.; Jackson, A.P. Trafficking and Cellular Distribution of Voltage-Gated Sodium Channels. *Traffic* **2008**, *9*, 17–26. [[CrossRef](#)]
30. Patino, G.A.; Isom, L.L. Electrophysiology and beyond: Multiple roles of Na⁺ channel β subunits in development and disease. *Neurosci. Lett.* **2010**, *486*, 53–59. [[CrossRef](#)]
31. Calhoun, J.D.; Isom, L.L. The Role of Non-pore-Forming β Subunits in Physiology and Pathophysiology of Voltage-Gated Sodium Channels. *Handb. Exp. Pharmacol.* **2014**, *221*, 51–89. [[CrossRef](#)]
32. Catterall, W.A. Structure and function of voltage-gated ion channels. *Annu. Rev. Biochem.* **1995**, *64*, 493–531. [[CrossRef](#)] [[PubMed](#)]
33. Isom, L.L.; De Jongh, K.S.; Patton, D.E.; Reber, B.F.; Offord, J.; Charbonneau, H.; Walsh, K.; Goldin, A.L.; Catterall, W.A. Primary structure and functional expression of the β 1 subunit of the rat brain sodium channel. *Science* **1992**, *256*, 839–842. [[CrossRef](#)] [[PubMed](#)]
34. Isom, L.L.; Scheuer, T.; Brownstein, A.B.; Ragsdale, D.S.; Murphy, B.J.; Catterall, W.A. Functional Co-expression of the 1 and Type IIA Subunits of Sodium Channels in a Mammalian Cell Line. *J. Biol. Chem.* **1995**, *270*, 3306–3312. [[CrossRef](#)] [[PubMed](#)]
35. McCormick, K.A.; Isom, L.L.; Ragsdale, D.; Smith, D.; Scheuer, T.; Catterall, W.A. Molecular Determinants of Na⁺Channel Function in the Extracellular Domain of the β 1 Subunit. *J. Biol. Chem.* **1998**, *273*, 3954–3962. [[CrossRef](#)] [[PubMed](#)]
36. Makita, N.; Bennett, P.B.; George, A.L., Jr. Molecular determinants of β 1 subunit-induced gating modulation in voltage-dependent Na⁺ channels. *J. Neurosci.* **1996**, *22*, 7117–7127. [[CrossRef](#)]
37. E Patton, D.; Isom, L.L.; A Catterall, W.; Goldin, A.L. The adult rat brain beta 1 subunit modifies activation and inactivation gating of multiple sodium channel alpha subunits. *J. Biol. Chem.* **1994**, *269*, 17649–17655.

38. Yu, E.J.; Ko, S.-H.; Lenkowski, P.W.; Pance, A.; Patel, M.K.; Jackson, A.P. Distinct domains of the sodium channel β 3-subunit modulate channel-gating kinetics and subcellular location. *Biochem. J.* **2005**, *392*, 519–526. [[CrossRef](#)] [[PubMed](#)]
39. Chen, C.; Cannon, S.C. Modulation of Na⁺ channel inactivation by the β 1 subunit: A deletion analysis. *Pflüg. Arch. Eur. J. Physiol.* **1995**, *431*, 186–195. [[CrossRef](#)]
40. Islas, A.A.; Sánchez-Solano, A.; Scior, T.; Millan-Perezpeña, L.; Salinas-Stefanon, E.M. Identification of Nav β 1 Residues Involved in the Modulation of the Sodium Channel Nav1.4. *PLoS ONE* **2013**, *8*, e81995. [[CrossRef](#)]
41. Scior, T.; Paiz-Candia, B.; Islas, Á.A.; Sánchez-Solano, A.; Peña, L.M.-P.; Mancilla-Simbros, C.; Salinas-Stefanon, E.M. Predicting a double mutant in the twilight zone of low homology modeling for the skeletal muscle voltage-gated sodium channel subunit beta-1 (Nav 1.4 β 1). *Comput. Struct. Biotechnol. J.* **2015**, *13*, 229–240. [[CrossRef](#)]
42. Sánchez-Solano, A.; Islas, A.A.; Scior, T.; Paiz-Candia, B.; Millan-Perezpeña, L.; Salinas-Stefanon, E.M. Characterization of specific allosteric effects of the Na⁺ channel β 1 subunit on the Nav1.4 isoform. *Eur. Biophys. J.* **2016**, *46*, 485–494. [[CrossRef](#)] [[PubMed](#)]
43. Chopra, S.S.; Watanabe, H.; Zhong, T.P.; Roden, D.M. Molecular cloning and analysis of zebrafish voltage-gated sodium channel beta subunit genes: Implications for the evolution of electrical signaling in vertebrates. *BMC Evol. Biol.* **2007**, *7*, 113. [[CrossRef](#)] [[PubMed](#)]
44. Isom, L.L. Sodium channel beta subunits: Anything but auxiliary. *Neuroscientist* **2001**, *7*, 42–54. [[CrossRef](#)] [[PubMed](#)]
45. Buffington, S.A.; Rasband, M.N. Na⁺ channel-dependent recruitment of Nav β 4 to axon initial segments and nodes of Ranvier. *J. Neurosci.* **2013**, *33*, 6191–6202. [[CrossRef](#)]
46. Chen, C.; Calhoun, J.D.; Zhang, Y.; Lopez-Santiago, L.; Zhou, N.; Davis, T.H.; Salzer, J.L.; Isom, L.L. Identification of the Cysteine Residue Responsible for Disulfide Linkage of Na⁺ Channel α and β 2 Subunits. *J. Biol. Chem.* **2012**, *287*, 39061–39069. [[CrossRef](#)]
47. Shen, H.; Zhou, Q.; Pan, X.; Li, Z.; Wu, J.; Yan, N. Structure of a eukaryotic voltage-gated sodium channel at near-atomic resolution. *Science* **2017**, *355*, eaal4326. [[CrossRef](#)]
48. Yan, Z.; Zhou, Q.; Wang, L.; Wu, J.; Zhao, Y.; Huang, G.; Peng, W.; Shen, H.; Lei, J.; Yan, N. Structure of the Nav 1.4- β 1 Complex from Electric Eel. *Cell* **2017**, *170*, 470–482.e11. [[CrossRef](#)]
49. Pan, X.; Li, Z.; Zhou, Q.; Shen, H.; Wu, K.; Huang, X.; Chen, J.; Zhang, J.; Zhu, X.; Lei, J.; et al. Structure of the human voltage-gated sodium channel Nav1.4 in complex with β 1. *Science* **2018**, *362*, eaau2486. [[CrossRef](#)]
50. Pan, X.; Li, Z.; Huang, X.; Huang, G.; Gao, S.; Shen, H.; Liu, L.; Lei, J.; Yan, N. Molecular basis for pore blockade of human Na⁺ channel Nav1.2 by the μ -conotoxin KIIIA. *Science* **2019**, *363*, 1309–1313. [[CrossRef](#)]
51. Shen, H.; Liu, D.; Wu, K.; Lei, J.; Yan, N. Structures of human Nav1.7 channel in complex with auxiliary subunits and animal toxins. *Science* **2019**, *363*, 1303–1308. [[CrossRef](#)]
52. Jiang, D.; Shi, H.; Tonggu, L.; El-Din, T.M.G.; Lenaeus, M.J.; Zhao, Y.; Yoshioka, C.; Zheng, N.; Catterall, W.A. Structure of the Cardiac Sodium Channel. *Cell* **2020**, *180*, 122–134.e10. [[CrossRef](#)] [[PubMed](#)]
53. Yu, F.H.; Westenbroek, R.E.; Silos-Santiago, I.; McCormick, K.A.; Lawson, D.; Ge, P.; Ferreria, H.; Lilly, J.; Distefano, P.S.; Catterall, W.A.; et al. Sodium Channel β 4, a New Disulfide-Linked Auxiliary Subunit with Similarity to β 2. *J. Neurosci.* **2003**, *23*, 7577–7585. [[CrossRef](#)] [[PubMed](#)]
54. Gilchrist, J.M.; Das, S.; Van Petegem, F.; Bosmans, F. Crystallographic insights into sodium-channel modulation by the β 4 subunit. *Proc. Natl. Acad. Sci. USA* **2013**, *110*, E5016–E5024. [[CrossRef](#)] [[PubMed](#)]
55. Namadurai, S.; Balasuriya, D.; Rajappa, R.; Wiemhöfer, M.; Stott, K.; Klingauf, J.; Edwardson, J.M.; Chirgadze, D.Y.; Jackson, A.P. Crystal structure and molecular imaging of the Nav channel β 3 subunit indicates a trimeric assembly. *J. Biol. Chem.* **2014**, *289*, 10797–10811. [[CrossRef](#)] [[PubMed](#)]
56. Das, S.; Gilchrist, J.; Bosmans, F.; Van Petegem, F. Binary architecture of the Nav1.2- β 2 signaling complex. *Elife* **2016**, *5*, e10960. [[CrossRef](#)]
57. McCormick, K.A.; Srinivasan, J.; White, K.; Scheuer, T.; Catterall, W.A. The Extracellular Domain of the β 1 Subunit Is Both Necessary and Sufficient for β 1-like Modulation of Sodium Channel Gating. *J. Biol. Chem.* **1999**, *274*, 32638–32646. [[CrossRef](#)]
58. Yereddi, N.R.; Cusdin, F.S.; Namadurai, S.; Packman, L.C.; Monie, T.P.; Slavny, P.; Clare, J.J.; Powell, A.J.; Jackson, A.P. The immunoglobulin domain of the sodium channel β 3 subunit contains a surface-localized disulfide bond that is required for homophilic binding. *FASEB J.* **2012**, *27*, 568–580. [[CrossRef](#)]

59. Shapovalov, M.V.; Dunbrack, R.L. A Smoothed Backbone-Dependent Rotamer Library for Proteins Derived from Adaptive Kernel Density Estimates and Regressions. *Struct.* **2011**, *19*, 844–858. [[CrossRef](#)]
60. Scouras, A.D.; Daggett, V. The dynamomics rotamer library: Amino acid side chain conformations and dynamics from comprehensive molecular dynamics simulations in water. *Protein Sci.* **2011**, *20*, 341–352. [[CrossRef](#)]
61. Pettersen, E.F.; Goddard, T.D.; Huang, C.C.; Couch, G.S.; Greenblatt, D.M.; Meng, E.C.; Ferrin, T.E. UCSF Chimera—a visualization system for exploratory research and analysis. *J. Comput. Chem.* **2004**, *25*, 1605–1612. [[CrossRef](#)]
62. Available online. *Met. Powder Rep.* **2008**, *63*, 11. [[CrossRef](#)]
63. Dolinsky, T.J.; Czodrowski, P.; Li, H.; Nielsen, J.E.; Jensen, J.H.; Klebe, G.; Baker, N. PDB2PQR: Expanding and upgrading automated preparation of biomolecular structures for molecular simulations. *Nucleic Acids Res.* **2007**, *35*, W522–W525. [[CrossRef](#)] [[PubMed](#)]
64. Baker, N.; Sept, D.; Joseph, S.; Holst, M.J.; McCammon, J.A. Electrostatics of nanosystems: Application to microtubules and the ribosome. *Proc. Natl. Acad. Sci. USA* **2001**, *98*, 10037–10041. [[CrossRef](#)]
65. Goddard, T.D.; Huang, C.C.; Meng, E.C.; Pettersen, E.F.; Couch, G.S.; Morris, J.H.; Ferrin, T.E. UCSF ChimeraX: Meeting modern challenges in visualization and analysis. *Protein Sci.* **2017**, *27*, 14–25. [[CrossRef](#)]
66. Microsoft Corporation. Microsoft Excel. Available online: <https://office.microsoft.com/excel> (accessed on 20 May 2016).
67. Hermann, J.C.; Marti-Arbona, R.; Fedorov, A.A.; Fedorov, E.; Almo, S.C.; Shoichet, B.K.; Raushel, F.M. Structure-based activity prediction for an enzyme of unknown function. *Nature* **2007**, *448*, 775–779. [[CrossRef](#)] [[PubMed](#)]
68. Zahiri, J.; Bozorgmehr, J.H.; Masoudi-Nejad, A. Computational Prediction of Protein–Protein Interaction Networks: Algorithms and Resources. *Curr. Genom.* **2013**, *14*, 397–414. [[CrossRef](#)]
69. Ezkurdia, I.; Bartoli, L.; Fariselli, P.; Casadio, R.; Valencia, A.; Tress, M.L. Progress and challenges in predicting protein-protein interaction sites. *Briefings Bioinform.* **2008**, *10*, 233–246. [[CrossRef](#)]
70. Whisstock, J.; Lesk, A. Prediction of protein function from protein sequence and structure. *Q. Rev. Biophys.* **2003**, *36*, 307–340. [[CrossRef](#)]
71. Izidoro, S.; De Melo-Minardi, R.C.; Pappa, G.L. GASS: Identifying enzyme active sites with genetic algorithms. *Bioinformatics* **2014**, *31*, 864–870. [[CrossRef](#)]
72. Jacobson, M.P.; Kalyanaraman, C.; Zhao, S.; Tian, B. Leveraging structure for enzyme function prediction: Methods, opportunities, and challenges. *Trends Biochem. Sci.* **2014**, *39*, 363–371. [[CrossRef](#)]
73. Ma, B.; Elkayam, T.; Wolfson, H.; Nussinov, R. Protein-protein interactions: Structurally conserved residues distinguish between binding sites and exposed protein surfaces. *Proc. Natl. Acad. Sci. USA* **2003**, *100*, 5772–5777. [[CrossRef](#)] [[PubMed](#)]
74. Keskin, O.; Ma, B.; Nussinov, R. Hot Regions in Protein–Protein Interactions: The Organization and Contribution of Structurally Conserved Hot Spot Residues. *J. Mol. Biol.* **2005**, *345*, 1281–1294. [[CrossRef](#)] [[PubMed](#)]
75. Li, X.; Keskin, O.; Ma, B.; Nussinov, R.; Liang, J. Protein–Protein Interactions: Hot Spots and Structurally Conserved Residues often Locate in Complemented Pockets that Pre-organized in the Unbound States: Implications for Docking. *J. Mol. Biol.* **2004**, *344*, 781–795. [[CrossRef](#)] [[PubMed](#)]
76. Kruger, L.C.; Isom, L.L. Voltage-Gated Na⁺ Channels: Not Just for Conduction. *Cold Spring Harb. Perspect. Biol.* **2016**, *8*, a029264. [[CrossRef](#)] [[PubMed](#)]
77. Salvage, C.S.; Huang, C.L.H.; Jackson, A.P. Cell-Adhesion Properties of β -Subunits in the Regulation of Cardiomyocyte Sodium Channels. *Biomolecules* **2020**, *10*, 989. [[CrossRef](#)]
78. Isom, L.L.; Ragsdale, D.S.; De Jongh, K.S.; E Westenbroek, R.; Reber, B.F.; Scheuer, T.; Catterall, W. Structure and function of the beta 2 subunit of brain sodium channels, a transmembrane glycoprotein with a CAM motif. *Cell* **1995**, *83*, 90121–90123. [[CrossRef](#)]
79. Molinarolo, S.; Granata, D.; Carnevale, V.; Ahern, C.A. Mining Protein Evolution for Insights into Mechanisms of Voltage-Dependent Sodium Channel Auxiliary Subunits. *Handb. Exp. Pharmacol.* **2018**, *246*, 33–49. [[CrossRef](#)]
80. Zhu, W.; Voelker, T.L.; Varga, Z.; Schubert, A.R.; Nerbonne, J.M.; Silva, J. Mechanisms of noncovalent β subunit regulation of NaV channel gating. *J. Gen. Physiol.* **2017**, *149*, 813–831. [[CrossRef](#)]

81. Messner, D.J.; Catterall, W. The sodium channel from rat brain. Separation and characterization of subunits. *J. Boil. Chem.* **1985**, *260*, 10597–10604.
82. Morgan, K.; Stevens, E.B.; Shah, B.; Cox, P.J.; Dixon, A.K.; Lee, K.; Pinnock, R.D.; Hughes, J.; Richardson, P.J.; Mizuguchi, K.; et al. beta 3: An additional auxiliary subunit of the voltage-sensitive sodium channel that modulates channel gating with distinct kinetics. *Proc. Natl. Acad. Sci. USA* **2000**, *97*, 2308–2313. [[CrossRef](#)]
83. Glass, W.G.; Duncan, A.L.; Biggin, P.C. Computational Investigation of Voltage-Gated Sodium Channel β 3 Subunit Dynamics. *Front. Mol. Biosci.* **2020**, *7*, 40. [[CrossRef](#)] [[PubMed](#)]
84. Namadurai, S.; Yereddi, N.R.; Cusdin, F.S.; Huang, C.L.-H.; Chirgadze, D.Y.; Jackson, A.P. A new look at sodium channel β subunits. *Open Boil.* **2015**, *5*, 140192. [[CrossRef](#)] [[PubMed](#)]
85. Lenkowski, P.W.; Shah, B.S.; E Dinn, A.; Lee, K.; Patel, M.K. Lidocaine block of neonatal Nav1.3 is differentially modulated by co-expression of β 1 and β 3 subunits. *Eur. J. Pharmacol.* **2003**, *467*, 23–30. [[CrossRef](#)]
86. Ragsdale, D.; McPhee, J.; Scheuer, T.; Catterall, W. Molecular determinants of state-dependent block of Na⁺ channels by local anesthetics. *Science* **1994**, *265*, 1724–1728. [[CrossRef](#)] [[PubMed](#)]
87. Ferrera, L.; Moran, O. β 1-subunit modulates the Nav1.4 sodium channel by changing the surface charge. *Exp. Brain Res.* **2006**, *172*, 139–150. [[CrossRef](#)]
88. Kinch, L.N.; Grishin, N.V. Evolution of protein structures and functions. *Curr. Opin. Struct. Biol.* **2002**, *12*, 400–408. [[CrossRef](#)]
89. Starr, T.; Thornton, J.W. Epistasis in protein evolution. *Protein Sci.* **2016**, *25*, 1204–1218. [[CrossRef](#)]
90. Kauvar, L.M.; O Villar, H. Deciphering cryptic similarities in protein binding sites. *Curr. Opin. Biotechnol.* **1998**, *9*, 390–394. [[CrossRef](#)]
91. Russell, R.B.; Sasieni, P.D.; Sternberg, M.J. Supersites within superfolds. Binding site similarity in the absence of homology 1 Edited by J. Thornton. *J. Mol. Boil.* **1998**, *282*, 903–918. [[CrossRef](#)]
92. Spitzer, R.; Cleves, A.E.; Varela, R.; Jain, A.N. Protein function annotation by local binding site surface similarity. *Proteins Struct. Funct. Bioinform.* **2013**, *82*, 679–694. [[CrossRef](#)]
93. Richards, F.M. Areas, volumes, packing and protein structure. *Annu. Rev. Biophys. Bioeng.* **1977**, *6*, 151–176. [[CrossRef](#)]
94. Gainza, P.; Sverrisson, F.; Monti, F.; Rodolà, E.; Boscaini, D.; Bronstein, M.M.; Correia, B.E. Deciphering interaction fingerprints from protein molecular surfaces using geometric deep learning. *Nat. Methods* **2019**, *17*, 1–9. [[CrossRef](#)] [[PubMed](#)]
95. Illergård, K.; Ardell, D.H.; Elofsson, A. Structure is three to ten times more conserved than sequence—A study of structural response in protein cores. *Proteins: Struct. Funct. Bioinform.* **2009**, *77*, 499–508. [[CrossRef](#)] [[PubMed](#)]
96. Sousounis, K.; E Haney, C.; Cao, J.; Sunchu, B.; Tsonis, P.A. Conservation of the three-dimensional structure in non-homologous or unrelated proteins. *Hum. Genom.* **2012**, *6*, 10. [[CrossRef](#)] [[PubMed](#)]
97. Gibrat, J.-F.; Madej, T.; Bryant, S.H. Surprising similarities in structure comparison. *Curr. Opin. Struct. Boil.* **1996**, *6*, 377–385. [[CrossRef](#)]
98. Caffrey, D.R.; Somaroo, S.; Hughes, J.D.; Mintseris, J.; Huang, E.S. Are protein–protein interfaces more conserved in sequence than the rest of the protein surface? *Protein Sci.* **2004**, *13*, 190–202. [[CrossRef](#)]
99. Grishin, N.V.; Phillips, M.A. The subunit interfaces of oligomeric enzymes are conserved to a similar extent to the overall protein sequences. *Protein Sci.* **1994**, *3*, 2455–2458. [[CrossRef](#)] [[PubMed](#)]
100. Binkowski, T.A.; Joachimiak, A. Protein Functional Surfaces: Global Shape Matching and Local Spatial Alignments of Ligand Binding Sites. *BMC Struct. Boil.* **2008**, *8*, 45. [[CrossRef](#)]
101. A Marshall, S.; Morgan, C.S.; Mayo, S.L. Electrostatics significantly affect the stability of designed homeodomain variants. *J. Mol. Boil.* **2002**, *316*, 189–199. [[CrossRef](#)]
102. Chothia, C.; Janin, J. Principles of protein–protein recognition. *Nature* **1975**, *256*, 705–708. [[CrossRef](#)]
103. Sheinerman, F.B.; Norel, R.; Honig, B. Electrostatic aspects of protein–protein interactions. *Curr. Opin. Struct. Boil.* **2000**, *10*, 153–159. [[CrossRef](#)]
104. Heifetz, A.; Katchalski-Katzir, E.; Eisenstein, M. Electrostatics in protein–protein docking. *Protein Sci.* **2002**, *11*, 571–587. [[CrossRef](#)] [[PubMed](#)]
105. Vizcarra, C.L.; Mayo, S.L. Electrostatics in computational protein design. *Curr. Opin. Chem. Boil.* **2005**, *9*, 622–626. [[CrossRef](#)] [[PubMed](#)]
106. Webb, B.; Sali, A. Protein Structure Modeling with MODELLER. *Adv. Struct. Saf. Stud.* **2014**, *1137*, 1–15. [[CrossRef](#)]

107. Lomize, M.A.; Lomize, A.L.; Pogozheva, I.D.; Mosberg, H.I. OPM: Orientations of Proteins in Membranes database. *Bioinformatics* **2006**, *22*, 623–625. [[CrossRef](#)] [[PubMed](#)]
108. Pedretti, A.; Villa, L.; Vistoli, G. VEGA—an open platform to develop chemo-bio-informatics applications, using plug-in architecture and script programming. *J. Comput. Mol. Des.* **2004**, *18*, 167–173. [[CrossRef](#)] [[PubMed](#)]
109. Sarvagalla, S.; Cheung, C.H.A.; Tsai, J.Y.; Hsiehd, H.P.; Coumar, M.S. Disruption of protein-protein interactions: Hot spot detection, structure-based virtual screening and in vitro testing for the anti-cancer drug target-surviving. *RSC. Adv.* **2016**, *6*, 31947–31959. [[CrossRef](#)]
110. Cukuroglu, E.; Gursoy, A.; Keskin, O. HotRegion: A database of predicted hot spot clusters. *Nucleic Acids Res.* **2011**, *40*, D829–D833. [[CrossRef](#)]

Sample Availability: Samples of the compounds are not available from the authors.



© 2020 by the authors. Licensee MDPI, Basel, Switzerland. This article is an open access article distributed under the terms and conditions of the Creative Commons Attribution (CC BY) license (<http://creativecommons.org/licenses/by/4.0/>).